What's in the sandwich? New P–T constraints for the (U)HP nappe stack of southern Dora-Maira Massif (Western Alps)

European Journal of Mineralogy

What's in the sandwich? New P-T constraints for the (U)HP nappe stack of southern Dora-Maira Massif (Western Alps)

--Manuscript Draft--

Manuscript Number:	ejm190006R1
Article Type:	Research paper
Full Title:	What's in the sandwich? New P-T constraints for the (U)HP nappe stack of southern Dora-Maira Massif (Western Alps)
Short Title:	Prograde P-T evolution of (U)HP units in the southern DMM
Corresponding Author:	Chiara Groppo University of Torino Torino, ITALY
Corresponding Author E-Mail:	chiara.groppo@unito.it
Order of Authors:	Chiara Groppo
	Simona Ferrando
	Manuele Gilio
	Serena Botta
	Francesco Nosenzo
	Gianni Balestro
	Andrea Festa
	Franco Rolfo
Abstract:	The Brossasco-Isasca Unit (BIU) of the southern Dora-Maira Massif (DMM), Western Alps, is one of the most studied ultra-high pressure (UHP) units in the world. However, the interpretation of UHP metamorphism in the BIU is still a highly debated and challenging issue. The structural and tectonometamorphic setting of the southern DMM is described in the literature as a tectonic “sandwich”, with the UHP unit in the middle, bounded by two high-pressure (HP) eclogitic units in the footwall (the San Chiaffredo Unit, SCU) and hanging wall (the Rocca Solei Unit, RSU), respectively. These three units are in turn sandwiched between two blueschist-facies units (the Pinerolo Unit, PU, at the bottom, and the Dronero-Sampeyre Unit, DSU, at the top). In contrast to the well-constrained P-T evolution of the BIU, peak P-T conditions for its bounding HP units are poorly constrained, most studies dating back to over 20 years ago and mostly relying on conventional thermobarometric methods. This study aims to update our knowledge about the P-T evolution experienced by the whole tectonometamorphic package of the southern DMM. For the first time, peak P-T conditions and prograde evolution for the five units (PU, SCU, BIU, RSU, DSU) forming the southern DMM tectonic “sandwich” are estimated using the same, internally consistent and therefore comparable, modern thermobarometric approaches. The study focuses on metapelites (i.e., garnet-bearing phengitic micaschists) and combines multi-equilibrium thermobarometry (Average PT) with the P-T pseudosection approach. Our results demonstrate that most of the southern DMM nappe stack (i.e., SCU, RSU and also the PU, that was originally considered as a blueschist-facies unit) experienced eclogite-facies metamorphism under similar peak P-T conditions (500-520°C, 20-24 kbar), and followed the same prograde path, suggesting similar burial mechanisms. The UHP BIU followed an early prograde evolution similar to that of the other eclogitic units of the southern DMM tectonic “sandwich”. The attainment of UHP peak conditions occurred through an earlier steep, almost isothermal increase in pressure and a later increase in temperature. The DSU is the only unit of the southern DMM nappe stack that did not experience eclogite-facies metamorphism (peak metamorphism at blueschist-facies conditions: 450-470 °C, 17-18 kbar) and it is separated from the eclogitic units by a shear zone (the Valmala Shear Zone), whose interpretation requires further studies. These new data represent the inescapable starting point for any conceptual model aiming for a deeper understanding of the subduction/exhumation processes of UHP

	continental units.
Keywords:	(U)HP metamorphism; southern Dora-Maira Massif; peak P-T conditions; prograde evolution; P-T pseudosections
Manuscript Region of Origin:	ITALY
Requested Editor:	Patrick Cordier, Editor-in-Chief
Additional Information:	
Question	**Response**
Author Comments:	
Response to Reviewers:	Dear Editor, the two reviewers and your own constructive comments have been carefully considered in order to improve the revised version of our manuscript. Please, find in the "ANSWERS TO EDITOR AND REVIEWERS".pdf file how and where the editor + reviewers comments have been incorporated in the manuscript. We hope that the manuscript now meets your approval for publication in European Journal of Mineralogy. With best regards, Chiara Groppo and co-authors

Cover Page

Title: **What's in the sandwich? New P-T constraints for the (U)HP nappe stack of southern Dora-Maira Massif (Western Alps)**

Running title

Prograde P-T evolution of (U)HP units in the southern DMM

Detailed plan of the article:

Corresponding author:

Chiara Groppo
Dept. of Earth Sciences, University of Torino
Via Valperga Caluso, 35, 10125 Torino (Italy)
chiara.groppo@unito.it
Tel. +39/0116705106
Fax: +39/0116705128

Title Page

What's in the sandwich? New P-T constraints for the (U)HP nappe stack of southern Dora-Maira Massif (Western Alps)

Chiara Groppo[1,2,*], Simona Ferrando[1], Manuele Gilio[1], Serena Botta[1], Francesco Nosenzo[1], Gianni Balestro[1], Andrea Festa[1], Franco Rolfo[1,2]

[1]Department of Earth Sciences, University of Torino, via Valperga Caluso 35, 10125 Torino, Italy

[2]CNR-IGG, via Valperga Caluso 35, 10125 Torino, Italy

*Corresponding author: chiara.groppo@unito.it

Abstract

The Brossasco-Isasca Unit (BIU) of the southern Dora-Maira Massif (DMM), Western Alps, is one of the most studied ultra-high pressure (UHP) units in the world. However, the interpretation of UHP metamorphism in the BIU is still a highly debated and challenging issue. The structural and tectonometamorphic setting of the southern DMM is described in the literature as a tectonic "sandwich", with the UHP unit in the middle, bounded by two high-pressure (HP) eclogitic units in the footwall (the San Chiaffredo Unit, SCU) and hanging wall (the Rocca Solei Unit, RSU), respectively. These three units are in turn sandwiched between two blueschist-facies units (the Pinerolo Unit, PU, at the bottom, and the Dronero-Sampeyre Unit, DSU, at the top). In contrast to the well-constrained P-T evolution of the BIU, peak P-T conditions for its bounding HP units are poorly constrained, most studies dating back to over 20 years ago and mostly relying on conventional thermobarometric methods. This study aims to update our knowledge about the P-T evolution experienced by the whole tectonometamorphic package of the southern DMM. For the first time, peak P-T conditions and prograde evolution for the five units (PU, SCU, BIU, RSU, DSU) forming the southern DMM tectonic "sandwich" are estimated using the same, internally consistent and therefore comparable, modern thermobarometric approaches. The study focuses on metapelites (*i.e.*, garnet-bearing phengitic micaschists) and combines multi-equilibrium thermobarometry (Average PT) with the P-T pseudosection approach. Our results demonstrate that most of the southern DMM nappe stack (*i.e.*, SCU, RSU and also the PU, that was originally considered as a blueschist-facies unit) experienced eclogite-facies metamorphism under similar peak P-T conditions (500-520°C, 20-24 kbar), and followed the same prograde path, suggesting similar burial mechanisms. The UHP BIU followed an early prograde evolution similar to that of the other eclogitic units of the southern DMM tectonic "sandwich". The attainment of UHP peak conditions occurred through an earlier steep, almost isothermal increase in pressure and a later increase in temperature. The DSU is the only unit of the southern DMM nappe stack that did not experience eclogite-facies metamorphism (peak metamorphism at blueschist-facies conditions: 450-470 °C, 17-18 kbar) and it is separated from the eclogitic units by a shear zone (the Valmala Shear Zone), whose interpretation requires further studies. These new data represent the inescapable starting point for any conceptual model aiming for a deeper understanding of the subduction/exhumation processes of UHP continental units.

Key-words

(U)HP metamorphism; southern Dora-Maira Massif; peak P-T conditions; prograde evolution; P-T pseudosections

1. Introduction

The first discovery, more than 30 years ago, of coesite in continental crustal rocks (Chopin, 1984; Smith, 1984), demonstrated the possibility for continental crust to reach ultra-high pressure (UHP) conditions. However, the geodynamic processes responsible for the formation and exhumation of continental UHP units are still debated (*e.g.*, Schenker *et al.*, 2015; Reuber *et al.*, 2016; Solarino *et al.*, 2018). Conceptual and numerical models that try to explain how a continental crustal unit can reach (and can be exhumed from) UHP conditions are calibrated against geological and petrological data available from the tectonic nappe stack which includes the UHP unit itself (*e.g.*, Li *et al.*, 2010; Burov *et al.*, 2014; Schamalholz *et al.*, 2014; Gerya, 2015; Schenker *et al.*, 2015). Precise knowledge of peak pressure and temperature (P-T) conditions experienced by both the UHP unit and its adjacent, often high-P (HP) units is therefore the crucial starting point to test the validity of the models (*e.g.*, Manzotti *et al.*, 2015, 2018).

The Brossasco-Isasca Unit (BIU) of the southern Dora-Maira Massif (DMM) in Western Alps, is one of the most studied UHP units worldwide and has been widely used in the past as a natural laboratory to discover new UHP minerals and to investigate metamorphic processes occurring during subduction at extreme pressures (*e.g.*, Chopin & Ferraris, 2003; Schertl & O'Brien, 2013 and references therein). The models assuming subduction of continental crust to mantle depths (*e.g.*, Chemenda *et al.*, 1995; Chopin, 2003; Stöckhert & Gerya, 2005; Gerya & Stöckhert, 2006; Yamato *et al.*, 2008; Butler *et al.*, 2013) were proposed after the discovery of coesite in the BIU. Decades later, the alternative idea of tectonic overpressure explaining UHP tectonics arose again in the southern DMM (*e.g.*, Ford *et al.*, 2006; Schmalholz *et al.*, 2014; Schmalholz & Duretz, 2015; Schenker *et al.*, 2015). More than 30 years after its discovery, the interpretation of UHP metamorphism in the BIU still remains a challenge for many generations of geoscientists.

In the southern DMM, the UHP BIU is tectonically sandwiched between two quartz-eclogite facies units, the lower San Chiaffredo Unit (SCU) and the upper Rocca Solei Unit (RSU), which are in turn bounded by two blueschist-facies units, the Pinerolo Unit (PU) at the bottom and the Dronero-Sampeyre Unit (DSU) at the top of the tectonometamorphic package (Fig. 1). In contrast to the well-constrained P-T evolution of the BIU (*e.g.*, Ferrando *et al.*, 2017 and references therein), peak P-T conditions for its adjacent Units are poorly constrained, most studies dating back to over 20 years ago and mostly relying on conventional thermobarometric methods (*e.g.*, Chopin *et al.*, 1991; Michard *et al.*, 1993; Compagnoni *et al.*, 1995). Notably, many of these studies, which still represent milestones for all those interested in the interpretation of the tectonometamorphic evolution and architecture of the southern DMM, were carried out by Christian Chopin and co-workers. It is therefore a great pleasure for us to contribute to this Special Issue dedicated to Christian Chopin, with the aim of updating his legacy, taking advantage of the modern petrological methods and exploiting the great amount of data collected by our group over last decades.

With these premises in mind, this study constrains the prograde-to-peak evolution experienced by the HP units bounding the UHP BIU. For the first time, peak P-T conditions for all five units (PU, SCU, BIU, RSU, DSU) forming the southern DMM tectonic "sandwich" (Compagnoni & Rolfo, 2003) are estimated using the same, internally consistent and therefore comparable, modern thermobarometric approaches. The study focuses on metapelites (*i.e.*, garnet-bearing phengitic micaschists) because they are widely exposed in all the investigated units and preserve the (U)HP assemblages well. Thermobarometric estimates are obtained combining multi-equilibrium thermobarometry (Average PT) and/or the P-T pseudosection approach applied to five samples (one for each unit). Concerning the HP units bounding the UHP BIU, our results confirm peak-T already known from the literature, but indicate systematically higher peak-P. The prograde path of the BIU is also significantly revised, with possible implications for the interpretation of burial mechanisms in the whole southern DMM tectonic "sandwich".

In our opinion, these new data represent the inescapable starting point for any model aimed at a deeper understanding of the processes responsible for the attainment and preservation of UHP conditions

in continental crust; however, further studies are needed in order to understand if (and how) the studied units shared part of their prograde evolution at HP to UHP conditions or if (and how) they were coupled during exhumation.

2. Geological setting

The Dora-Maira Massif (DMM) in the Western Alps, represents part of the subducted-exhumed European continental margin (*e.g.*, Michard *et al.*, 1996). It is now stacked in the Alpine orogenic wedge (Lardeaux *et al.*, 2006), wherein it was overthrust by meta-ophiolite units of the Piedmont Zone (Balestro *et al.*, 2018, and references therein). The southern portion of the DMM is a pile of imbricated thrust sheets, resulting from Alpine tectonic juxtaposition and metamorphic reworking of slices of Variscan continental crust and of Permian igneous bodies (*e.g.*, Vialon, 1966; Henry, 1990; Chopin *et al*., 1991; Michard *et al*., 1993, 1995; Turello, 1993; Sandrone *et al.,* 1993; Balestro *et al*., 1995; Compagnoni *et al*., 1995, 2012; Compagnoni & Rolfo, 1999, 2003; Groppo, 2002; Compagnoni *et al*., 2004, 2012; Botta, 2015; Nosenzo, 2018). Relics of both amphibolite-facies Variscan metamorphism and Permian contact metamorphism are locally still preserved (*e.g.*, Biino & Compagnoni, 1992; Compagnoni *et al*., 1995; Compagnoni & Rolfo, 2003; Groppo *et al*., 2006, 2007b).

In the area between the Po Valley to the north and the Maira Valley to the south, the following tectonometamorphic units are distinguished from the lower to the upper structural position (Fig. 1): (i) the Pinerolo Unit (PU) is a monometamorphic unit that experienced Alpine epidote-blueschist facies metamorphism (*e.g.*, Chopin *et al*., 1991; Avigad *et al*., 2003); (ii) the San Chiaffredo Unit (SCU) is a portion of pre-Alpine continental crust (Variscan amphibolite-facies basement intruded by Permian granitoids) that reached quartz-eclogite facies peak during Alpine metamorphism (Compagnoni & Rolfo, 2003); (iii) the Brossasco-Isasca Unit (BIU) is lithologically similar to the SCU but experienced Alpine peak P-T conditions in the coesite-eclogite facies (diamond stability field; *e.g.*, Schertl *et al*., 1991; Nowlan *et al*., 2000; Rubatto & Hermann, 2001; Hermann, 2003; Ferraris *et al*., 2005; Di Vincenzo *et al*., 2006; Castelli *et al*., 2007; Groppo *et al*., 2007a; Ferrando *et al*., 2009; Gauthiez-Putallaz *et al*., 2016); (iv) the Rocca Solei Unit, lithologically similar to the BIU and the SCU, experienced Alpine peak P-T conditions at quartz-eclogite facies conditions (Chopin *et al*., 1991; Matsumoto & Hirajima, 2000); (v) the Dronero-Sampeyre Unit (DSU) includes polymetamorphic schists (Henry, 1990; Chopin *et al*., 1991) and a monometamorphic Permian volcano-detrital sequence (Vialon, 1966; Chopin *et al*., 1991; Michard *et al*., 1995), both of which experienced Alpine peak P-T conditions at epidote-blueschist facies (Chopin *et al*., 1991). The DSU is separated from the structurally underlying RSU by a shear zone, hundreds of metres thick, consisting of the tectonic juxtaposition of meta-ophiolite and metasediment slices (Valmala Shear Zone; *i.e*., the "ophiolitiferous band" of Henry *et al*., 1993). The term "tectonic sandwich" is hereafter used to indicate the whole package of juxtaposed tectonometamorphic units of southern DMM described above. All these units have been overprinted by a late-Alpine greenschist-facies recrystallization, which pervasively reworked and extensively obliterated the former (U)HP metamorphic mineral assemblages.

Sample locations are reported in Fig. 1 and additional details are given in the Supplementary material.

3. Methods

3.1 Micro-X-ray fluorescence (μ-XRF) maps

Qualitative major element X–ray maps of the entire thin sections were acquired using a micro-XRF Eagle III–XPL spectrometer equipped with an EDS Si(Li) detector and with an EdaxVision32 microanalytical system at the Department of Earth Sciences, University of Torino. Operating conditions were: 100 ms counting time, 40 kV accelerating voltage, and a probe current of 900 μA. A spatial resolution of about 65 μm in both x and

y directions was used. Quantitative modal amounts of each mineral phase were obtained by processing the maps with the software Petromod (Cossio *et al*., 2002). For each sample, the processed X–ray maps are reported in Fig. 2. Additional microstructural details, at greater magnification, are given in Figs. 3-5. Mineral abbreviations are after Whitney & Evans (2010), except white mica (Wm) and phengite (Phe).

3.2 Mineral chemistry

The rock-forming minerals were analyzed with a Jeol JSMIT300LV Scanning Electron Microscope at the Department of Earth Sciences, University of Torino. The instrument was equipped with an energy dispersive spectrometry (EDS) Energy 200 system and an SDD X-Act3 detector (Oxford Inca Energy). Operating conditions were: 50 s counting time, 15 kV accelerating voltage, spot size 2 μm. SEM-EDS quantitative data were acquired and processed using the Microanalysis Suite Issue 12, INCA Suite version 4.01; natural mineral standards were used to calibrate the raw data; the φρZ correction (Pouchou & Pichoir, 1988) was applied. Tables SM1 and SM2-SM6, freely available online as Supplementary Material linked to this article on the GSW website of the journal, https://pubs.geoscienceworld.org/eurjmin/, summarize the compositional variations (Table SM1) and the representative chemical compositions for the main minerals in each sample; Figs. 6-7 and SM1 show the composition of garnet and phengite. For practical purposes, the term phengite is used in the following to indicate phengitic white mica with Si > 3.20 a.p.f.u. (on the basis of 11 oxygens), whereas muscovite is used for phengitic white mica with Si < 3.20 a.p.f.u.

3.3 Pseudosection modelling

The pseudosection modeling approach was applied to each metapelite sample, excluding DM1565. Bulk-rock composition of each sample (Table 1) was calculated by combining estimated mineral modes with mineral chemistry (see above). Determination of an effective bulk composition for sample DM1565 (DSU) was problematic because: (i) the fine-grained nature of Alpine Grt_2 hampered its correct quantification from micro-XRF maps; (ii) the presence of pre-Alpine garnet porphyroblasts (Grt_1), that should be subtracted from the bulk-composition effectively reacting during Alpine metamorphism, makes the conventional bulk-rock analysis (*e.g*., XRF or ICP-MS) not suitable.

For each considered sample, three P-T isochemical phase diagrams have been calculated (*i.e*., a total of 12 pseudosections) considering the fractionation effects on the bulk-composition due to the growth of zoned garnet porphyroblasts. Each pseudosection was used to model: (i) P-T conditions for garnet core growth (measured bulk-composition: MBC), (ii) P-T conditions for garnet mantle growth (MBC minus garnet cores), and (iii) P-T conditions for garnet rim growth (MBC minus garnet cores + mantles) (Table 1).

The P-T isochemical phase diagrams were calculated in the system MnNKCFMASTOH (MnO-Na_2O-K_2O-CaO-FeO-MgO-Al_2O_3-SiO_2-TiO_2-Fe_2O_3-H_2O), except for sample DM1281 (BIU), for which Fe^{3+} was neglected, because Fe^{3+}-rich oxides are absent and the amount of Fe^{3+} in the analyzed minerals is very low. The pseudosections were calculated using Perplex 6.8.1 (version March 2018; Connolly, 1990, 2005, 2009), the internally consistent thermodynamic dataset of Holland & Powell (2011) (ds62) and the equation of state for H_2O of Holland & Powell (1998). The following solution models were used: garnet, chlorite, chloritoid, staurolite, white mica, biotite and ilmenite (White *et al*., 2014), omphacite (Green *et al*., 2007), amphibole (Green *et al*., 2016), carpholite (Smye *et al*., 2010), feldspar (Fuhrman & Lindsley, 1988) and epidote (Holland & Powell, 2011). Quartz, lawsonite, kyanite, rutile and titanite were considered as pure phases. The fluid was usually considered as pure H_2O ($a H_2O$=1), but a reduced $a H_2O$=0.4 was considered in the pseudosection that models the garnet rim growth in DM1281 (BIU) because experimental and fluid inclusions studies (Sharp *et al*., 1993; Hermann, 2003; Ferrando *et al*., 2009) demonstrated that, at the UHP peak, the activity of H_2O was strongly reduced by the abundance of dissolved species.

3.4 Optimal thermobarometry

The THERMOCALC "Average PT" (AvPT) method (*i.e.*, "Optimal thermobarometry": Powell & Holland, 1994) was applied to all the samples. THERMOCALC v3.40 and the Holland & Powell (2011) dataset (ds62) were used. Activity-composition relationships were calculated using the software AX. The method was applied to the peak assemblage for all the samples, except sample DM1281 (BIU), for which it was applied to the late prograde assemblage (see Section 4.3). Used sets of mineral compositions and of independent reactions are given in Tables SM2-SM7. AvPT results are discussed in terms of weighted means (*i.e.*, values with smaller errors contribute more than values with larger errors) and are presented in Table 2.

4. Petrography and mineral chemistry

4.1 Sample DM 1485 (PU)

This medium- to coarse-grained micaschist consists of white mica (mostly phengite; 42%), garnet (20%), chlorite (19%), quartz (13%) and minor chloritoid (2%) (Fig. 2). Retrograde chlorite, plagioclase (3%) and minor biotite, as well as accessory magnetite, rutile and ilmenite also occur. The main foliation (S_m) is defined by preferred orientation of phengite and chlorite, that form continuous pluri-mm -thick layers alternated with discontinuous pluri-mm -thick quartzitic layers (Fig. 2). An earlier schistosity (S_{m-1}), defined by the preferred orientation of white mica and chlorite, is still preserved in microlithons.

Garnet porphyroblasts, up to several millimetres in size, are syn-kinematic with respect to S_m and show a snow-ball structure (Fig. 3a); the rotated internal foliation, continuous with the external S_m, is defined by inclusions of quartz, relict chloritoid, and minor white mica and chlorite (Fig. 3b). Quartz, phengite and chlorite occur in the pressure shadows of garnet. Garnet porphyroblasts are strongly zoned (Fig. 6a and Table SM1), with a reddish core and a pinkish rim.

Phengite defines the S_m and rarely occurs, in association with paragonite and relict chloritoid, in polymineralic inclusions within garnet core and mantle (Fig. 3b). A few retrograde muscovite flakes occur in matrix and in polymineralic inclusions within garnet. Paragonite is only observed in polymineralic inclusions in garnet, always associated with (or replacing) chloritoid; its prograde vs. retrograde nature is ambiguous. Bluish-greenish chloritoid is only preserved as inclusions in garnet porphyroblasts (Fig. 3a,b), but not in the matrix. Its composition changes according to the microstructural position within garnet (Table SM1). Chlorite is mostly in equilibrium with S_m, but a late chlorite generation replaces garnet along fractures. Chlorite rim is locally partially replaced by fine-grained biotite. Plagioclase (albite to oligoclase) occurs as large (pluri-mm) blasts overgrowing the S_m and it is thus interpreted as a retrograde phase.

Among the accessories, retrograde mm-sized magnetite exclusively occurs in the matrix (Fig. 2). Rutile and ilmenite within garnet core, mantle and rim appear in equilibrium, whereas in the matrix rutile is rimmed by ilmenite.

4.2 Sample DM1667c (SCU)

This garnet-bearing phengitic micaschist has a strongly heterogeneous grain size. It shows a mm-thick banded structure, with continuous medium- to coarse-grained phengite-rich layers alternating with fine- to medium-grained discontinuous quartz-rich layers (Fig. 2). It consists of white mica (mostly phengite: 42%), garnet (30%), quartz (18%) and minor chloritoid (1%). Retrograde chlorite (7%), epidote (1%), minor biotite, and accessory magnetite, rutile, ilmenite, tourmaline and apatite also occur. The main foliation (S_m) is defined by the preferred orientation of white mica.

Garnet porphyroblasts are centimetres to pluri-cm in size in the coarse-grained layers, and millimetres to pluri-mm in the finer-grained layers (Fig. 2). Garnet is pre- to syn-kinematic with respect to the

S_m, being mostly enveloped by the main schistosity, but with the rim that appears in equilibrium with it. Garnet porphyroblasts are microstructurally and chemically zoned (Fig. 6b). Garnet core and mantle are large, often asymmetric, and crowded with inclusions, whereas rim is thin and with few inclusions. Fine-grained inclusions in garnet core consist of epidote (Fig. 3d), chlorite and chloritoid; inclusions in garnet mantle are medium-grained and mostly consist of chloritoid (Fig. 3c) and white mica. Garnet rim includes few phengite flakes and box-shaped pseudomorphs after former lawsonite, consisting of a fine-grained aggregate of epidote, muscovite, paragonite and chlorite (Fig. 3e). A thin (100-300 μm) and discontinuous outer rim slightly enriched in Mn has been interpreted as due to local retrograde re-equilibration.

Phengite defines the S_m and is locally included in garnet. Less abundant retrograde muscovite overgrows the main foliation and replaces chloritoid inclusions within garnet. Paragonite only occurs as inclusion in garnet, associated with (or replacing) chloritoid, and as pseudomorphs after probable lawsonite; therefore, it has been interpreted as both prograde and retrograde phase. Chloritoid is mostly included in garnet mantle (Fig. 3c), rarely in core and rim, and it is absent from the matrix. It is locally partially to completely replaced by an aggregate of white mica (muscovite ± phengite + paragonite) (Fig. 3c).

Epidote and chlorite occur in two different generations. Prograde epidote (often with an allanitic core) and chlorite are included in garnet core and mantle (Fig. 3d). Retrograde epidote occurs as few fine-grained idioblasts in matrix and in pseudomorphs after lawsonite included in garnet rim, whereas late chlorite mostly replaces garnet porphyroblasts along fractures and rims. Late biotite partially replaces white mica and chlorite at their rims.

Among accessories, mm-sized retrograde magnetite only occurs in the matrix. Rutile and ilmenite occur as inclusions within garnet porphyroblasts; in the matrix rutile is rimmed by ilmenite. Apatite and tourmaline are included in garnet.

4.3 Sample DM1281 (BIU)

This sample consists of white mica (mostly phengite, 41%), quartz (24%), garnet (21%), kyanite (10%), jadeite (3%) and minor chloritoid, staurolite and chlorite (Fig. 2). Albite and pyrophyllite are retrograde phases, whereas rutile, tourmaline and apatite are the main accessory minerals. The grain size is markedly heterogeneous, with pluri-mm garnet and kyanite porphyroblasts set in a fine-grained matrix mostly consisting of phengite and quartz (Fig. 2). The main schistosity (S_m) is defined by mm-thick, continuous phengitic layers, alternating with discontinuous quartzitic layers of similar thickness.

Garnet porphyroblasts are microstructurally and chemically zoned (Fig. 6c). Garnet core and mantle are large, often asymmetric, and crowded with inclusions, whereas rim is thin and with few inclusions (Fig. 4a). Garnet rim appears in equilibrium with S_m. Inclusions in garnet core are fine-grained and polymineralic; garnet mantle includes both fine-grained polymineralic inclusions and medium-grained monocrystalline inclusions; garnet rim contains few medium-grained monocrystalline inclusions. Polymineralic inclusions in garnet core mostly consist of chloritoid, paragonite, chlorite, staurolite and rare muscovite, whereas those observed in garnet mantle contain also kyanite and does not contain potassic white mica (Fig. 4d,e). Monocrystalline inclusions in garnet mantle are represented by pseudomorphs after jadeite and glaucophane (Fig. 4f, g), kyanite and quartz, whereas those in garnet rim consist of kyanite, phengite and quartz. Polycrystalline aggregates of quartz surrounded by radial cracks, interpreted as deriving from inversion of coesite, are located at the transition between garnet mantle and rim (Fig. 4a).

Phengite defines the S_m and is locally included in garnet rim. Retrograde muscovite is scarce and its occurrence is limited to the pseudomorphs after jadeite and glaucophane. A few prograde muscovite flakes are preserved in the polymineralic inclusions within garnet core. Paragonite is common in the polymineralic inclusions hosted within garnet core and mantle (Fig. 4e), where it probably has a prograde nature.

At least three different generations of kyanite have been recognized: i) large (pluri-mm) porphyroblasts enveloped by the main foliation (Fig. 4b); ii) smaller idioblasts in equilibrium with the S_m (Fig. 4b); iii) local very fine-grained acicular crystals rimming the large kyanite porphyroblasts. Jadeite and glaucophane are not preserved, but are pseudomorphically replaced by retrograde phases. Pseudomorphs after jadeite, occurring both in the matrix (Fig. 4c) and as inclusion in garnet mantle (Fig. 4g), consist of a very fine-grained aggregate of albite + pyrophyllite + muscovite. Lozenge-shaped pseudomorphs after glaucophane have been observed only as inclusions in garnet mantle (Fig. 4f) and consist of a very fine-grained aggregate of paragonite + muscovite + minor biotite.

Chloritoid, chlorite and staurolite only occur in the fine-grained polymineralic inclusions within garnet core and mantle (Fig. 4d,e). Chlorite is a prograde phase and the X_{Mg} of the chlorite included in garnet mantle is higher than that of the chlorite included in garnet core (Table SM1). Chloritoid is generally associated with paragonite and chlorite. Staurolite is only present as inclusion in both garnet core and mantle, where it mostly occurs in association with kyanite, paragonite and chlorite, more rarely with chloritoid. Microstructural relationships clearly show that staurolite grew at the expense of kyanite, often preserved as rounded relics partially rimmed by staurolite (Fig. 4e).

Accessory rutile, tourmaline and apatite occur in the matrix and as inclusion in garnet

4.4 Sample DM1504 (RSU)

This fine- to coarse-grained, garnet-bearing phengitic micaschist consists of white mica (mostly phengite, 49 % and paragonite, 6%), quartz (20%), chloritoid (12%) and garnet (8%) (Fig. 2), with minor amounts of glaucophane and jadeite (almost completely replaced by retrograde phases). Retrograde chlorite (3%), epidote (1%) and biotite, and accessory rutile, ilmenite, magnetite and apatite also occur. The main foliation (S_m) is defined by mm- to pluri-mm -thick, continuous, micaceous layers alternated with mm-thick, discontinuous, quartzitic layers. Relics of an earlier S_{m-1} schistosity are locally preserved in microlithons and are defined by the alignment of white mica.

Mm- to pluri-mm -sized garnet porphyroblasts are partially enveloped by the S_m, but their rim appears in equilibrium with S_m (*i.e.*, garnet is pre- to syn-kinematic with respect to S_m). They include an internal rotated foliation mostly defined by quartz and chloritoid. Garnet core and mantle are large and rich of inclusions, whereas garnet rim is thin and with few inclusions (Fig. 5a-c). Inclusions in garnet are either polymineralic or monocrystalline. Polymineralic inclusions mostly consist of chloritoid + white micas (phengite ± paragonite ± muscovite) (Fig. 5b). Relics of glaucophane + jadeite, partially replaced by paragonite + albite ± muscovite, have been observed at the transition between garnet mantle and garnet rim (Fig. 5b). Garnet core and mantle locally include tabular-shaped aggregates of epidote + quartz + paragonite or phengite (Fig. 5c), possibly representing pseudomorphs after former lawsonite. Monocrystalline inclusions mostly consist of quartz, chloritoid and minor phengite.

Phengite defines the S_m and is locally included in garnet and chloritoid. Retrograde paragonite and muscovite occur both in the matrix and as inclusions in garnet. In the matrix, paragonite forms large flakes statically overgrowing the S_m (Fig. 2). When included in garnet, paragonite and muscovite generally replace other phases, such as glaucophane, jadeite or chloritoid. Chloritoid occurs both in the matrix and as inclusion in garnet (Fig. 5a). In the matrix, it forms medium-grained bluish-greenish nematoblasts aligned with the S_m and it is slightly zoned. Rare glaucophane and jadeite relics are included in garnet mantle/rim (Fig. 5b).

Epidote, chlorite, albite and biotite are retrograde phases. Epidote within garnet occurs in tabular-shaped aggregates, in association with quartz and white micas, interpreted as deriving from former lawsonite (Fig. 5c). In the matrix, it forms few fine-grained idioblasts, often with an allanitic core. Aggregates of chlorite statically overgrows the S_m and replaces garnet along fractures and at the rim. Its rim is locally replaced by biotite. Albite occurs as replacement of jadeite and glaucophane.

Rutile mostly occurs as inclusion in garnet, whereas it is pervasively replaced by ilmenite in the matrix. Retrograde magnetite is fine-grained and widespread in the matrix, and it is strongly oxidized. Apatite occurs as relatively large grains both in the matrix and included in garnet.

4.5 Sample DM1565 (DSU)

This garnet-bearing phengitic micaschist consists of white mica (mostly phengite, 54% and paragonite, 8%), quartz (26%), garnet (5%) and chloritoid (3%) (Fig. 2). Retrograde chlorite (3%) and biotite and accessory rutile, ilmenite and tourmaline also occur. The main schistosity (S_m) is defined by pluri-mm thick, continuous, micaceous layers alternating with mm-thick quartzitic layers. Large (pluri-mm) garnet porphyroblasts are preferentially set in the fine-grained micaceous layers (Fig. 2).

In contrast to the other samples, this metapelite preserves mineralogical evidence of a polymetamorphic evolution. Two different garnet generations can be, in fact, recognized: (i) large porphyroblasts (Fig. 5d) enveloped by the S_m, interpreted as amphibolite-facies Variscan garnets (Grt_1); (ii) small (ca. 100 μm) idioblasts in equilibrium with S_m and a thin and discontinuous corona around porphyroblastic Grt_1 (Fig. 5e), both interpreted as Alpine garnets (Grt_2). The strongly-fractured Grt_1 is chemically zoned (Table SM1). Locally it is poikiloblastic and includes quartz, white mica, ilmenite and minor staurolite, now replaced by fine-grained pseudomorphic aggregates of white mica + chloritoid. The small Grt_2 idioblasts are also zoned and include very fine-grained quartz (Fig. 6e and Table SM1).

Phengite defines the S_m and it also occurs at the rim of the chloritoid-bearing pseudomorphs after former staurolite. Minor retrograde muscovite and paragonite occur in the matrix. Chloritoid mostly constitutes large (pluri-mm) fine-grained aggregates enveloped by the S_m and interpreted as pseudomorphs after pre-Alpine porphyroblastic staurolite (Fig. 5f) (see also Henry, 1990; Chopin *et al.*, 1991). These pseudomorphs also contain white mica (phengite + muscovite + paragonite), generally concentrated toward the rim. Chloritoid also forms minor idioblasts aligned with the S_m or partially overgrowing it.

Retrograde chlorite occurs as large flakes statically overgrowing the S_m and partially replacing garnet at the rim and along fractures. Biotite is limited to late and discontinuous shear bands crosscutting the main foliation. Accessory ilmenite is included in pre-Alpine garnet (Grt_1) and is rimmed by rutile, if it communicates with the external matrix through fractures. In the matrix, rutile is rimmed by ilmenite.

5. Resulting P-T evolution

The prograde-to-peak P-T evolution of the PU, SCU, BIU and RSU samples was constrained using the pseudosection approach and on the basis of the predicted stability fields of the observed mineral assemblages, combined with garnet, chloritoid and phengite compositional isopleths. The results of thermodynamic modelling show that the fractionation effects on the bulk-composition due to the growth of zoned garnet porphyroblasts are generally minor during the initial growth of garnet (*i.e.*, after the fractionation of garnet core). However, they become significant after the fractionation of both garnet core and mantle. The general topology of the calculated pseudosections for all samples is similar as far as the relationships between the main phases of interest is concerned, and is in line with previous studies related on phase equilibria modeling in the same system (*e.g.*, Guiraud *et al.*, 1990; Proyer, 2003; Wei & Powell, 2004, 2006; Smye *et al.*, 2010; Manzotti *et al.*, 2015): (i) garnet is always stable over a large range of P-T conditions, whereas chlorite is limited to P <18-25 kbar; (ii) chloritoid is stable at T<550-600°C, and kyanite is instead stable at increasing temperature (see Smye *et al.*, 2010); (iii) paragonite, glaucophane and jadeite represent the Na-rich phases stable at lower, intermediate and higher pressure, respectively.

The Average PT approach of THERMOCALC was further applied to peak assemblages for the PU, SCU, RSU and DSU samples and to the late prograde assemblage for the BIU sample. In the following, the results of both approaches are summarized.

5.1 Sample DM1485 (PU)

The observed prograde and peak assemblage (Qz + Phe + Grt + Chl + Cld + Rt + Ilm) is not modeled in the P-T region of interest because chloritoid is always predicted to be stable with a Na-rich phase (either paragonite or glaucophane), which was not observed in the studied sample. However, the occurrence of large oligoclase porphyroblasts in the matrix statically overgrowing the main foliation suggests that one or more Na-rich phases (e.g. glaucophane, paragonite) was likely stable in the prograde and peak assemblages and it is not preserved. The glaucophane/paragonite-bearing assemblage (Qz + Phe + Grt + Chl + Cld + Gln/Pg + Rt + Ilm) is modeled in a wide range of P-T conditions (450-570°C, 10-25 kbar) (Fig. 8).

Prograde and peak P-T conditions are more tightly constrained by the intersection of compositional isopleths. Specifically: (i) early prograde P-T conditions are constrained at 480-495°C, 19-21 kbar using compositions of garnet core ($Sps_5Prp_6Grs_8Alm_{80}$) and of its inclusions of chloritoid (X_{Mg}=0.11) and phengite (Si=3.48 a.p.f.u.) (Fig. 8a); (ii) late prograde P-T conditions are constrained at 490-505°C, 20-22 kbar using the compositions of garnet mantle ($Sps_{2.5}Prp_8Grs_{7.5}Alm_{81}$) and of its inclusions of chloritoid (X_{Mg}=0.15) and phengite (Si=3.44-3.45 a.p.f.u.) (Fig. 8b); (iii) peak P-T conditions are estimated at 500-515°C, 20-23 kbar using the compositions of garnet rim ($Sps_{0.5}Prp_{11}Grs_{11}Alm_{78}$), of its chloritoid inclusions (X_{Mg}=0.18) and of matrix phengite (Si=3.38-3.51 a.p.f.u.) (Fig. 8c).

The AvPT approach applied to four different sets of mineral compositions gives peak P-T conditions of 496 ± 7 °C, 19.0 ± 0.7 kbar (Table 2), consistent with the results of pseudosection modeling (Fig. 8c).

5.2 Sample DM1667c (SCU)

Although glaucophane was not observed in prograde and peak assemblages, the modeled pseudosections predict its stability over a large P-T interval. However, the predicted modal amount of glaucophane is so low (< 5 vol%) that its (former) occurrence could likely have been overlooked. Ignoring glaucophane, the observed early prograde (Qz + Phe + Grt_C + Chl + Cld + Ep + Rt + Ilm) and late prograde (Qz + Phe + Grt_M + Cld ± Chl ± Ep/Lws + Rt + Ilm) assemblages are modeled by large tri- and quadri-variant fields at 420-500°C, 12-17 kbar and 400-500°C, 14-25 kbar, respectively (Fig. 9). Garnet, chloritoid and phengite compositional isopleths allow to further constrain the prograde P-T conditions: (i) early prograde conditions are constrained at 460-470°C, 17-19 kbar using the compositions of garnet core ($Sps_5Prp_{3.5}Grs_{26}Alm_{65}$) and its inclusions of phengite (Si=3.34-3.46 a.p.f.u.) (Fig. 9a); (ii) late prograde P-T conditions are constrained at 480-490°C, 19-21 kbar using the compositions of garnet mantle ($Sps_{2.5}Prp_5Grs_{24}Alm_{68}$) and of its inclusions of chloritoid (X_{Mg}=0.20) and phengite (Si=3.40-3.49 a.p.f.u.) (Fig. 9b). Although garnet core includes epidote, its growth is predicted to occur within the lawsonite stability field, but close to the Ep-out boundary.

The observed peak assemblage (Qz + Phe + Grt_R + Cld + Lws + Rt + Ilm) is modeled by a relatively small quadri-variant field at 450-520°, 22-27 kbar. The intersection of compositional isopleths for garnet rim ($Sps_{0.8}Prp_{10}Grs_{18}Alm_{74}$) and its inclusions of chloritoid (X_{Mg}=0.20) and phengite (Si=3.36-3.43 a.p.f.u.) defines peak P-T conditions at 500-520°C, 21-24 kbar (Fig. 9c). The AvPT approach applied to four different sets of mineral compositions gives peak P-T conditions of 512 ± 8 °C, 21.9 ± 0.9 kbar (Table 2), consistent with the results of pseudosection modeling (Fig. 9c).

5.3 Sample DM1281 (BIU)

Garnet core and its inclusions define the early prograde assemblage (Qz + Phe + Grt_C + Cld + Pg+ Chl + Rt). Staurolite is not considered as part of this assemblage due to its supposed retrograde nature (see microstructural relationships presented in Section 4.3). This assemblage is modeled by a quadri-variant field at 450-570°C, 10-18 kbar. The best fit between observed and modeled garnet ($Sps_{6.5}Prp_{12}Grs_6Alm_{74}$), chloritoid ($X_{Mg}$=0.25) and chlorite ($X_{Mg}$=0.62) compositions constrains P-T conditions for the growth of garnet core at 520-540°C, 16-23 kbar (Fig. 10a), in the Qz + Phe + Grt + Cld + Pg± Chl ± Gln + Rt fields. These P-T conditions are at significantly lower T and higher P than the predicted stability field of staurolite, further confirming that staurolite is not compatible with the early prograde assemblage (see Section 4.3).

The late prograde assemblage consists of garnet mantle and its inclusions (Qz/Coe + Phe + Grt_M + Cld + Pg+ Ky + Jd + Gln + Rt); once again staurolite is not considered as part of this assemblage. Pseudomorphs after coesite are hosted in the outermost mantle domain, at the transition between Grt_M and Grt_R, suggesting that garnet mantle already grew at UHP conditions. The coexistence of chloritoid + kyanite constrains the temperature to a very narrow range (540-560°C), whereas the coexistence of jadeite, glaucophane and paragonite in the same garnet domain limits the pressures to the interval 24-28 kbar, *i.e.*, close to the transition between paragonite-bearing and jadeite-bearing fields (Fig. 10b). The modeled garnet ($Sps_{1.5}Prp_{19}Grs_2Alm_{76}$) and chloritoid ($X_{Mg}$=0.30) compositional isopleths intersect within these fields and tightly constrain the late prograde P-T conditions at 540-560°C, 25-30 kbar, *i.e.*, at the transition between the quartz and coesite stability fields (Fig. 10b). This is consistent with the observed occurrence of polycrystalline aggregates of quartz after coesite at the transition between garnet mantle and rim. The AvPT approach applied to four different sets of mineral compositions gives late prograde P-T conditions of 557 ± 5 °C, 27.4 ± 0.4 kbar (Table 2), consistent with the pseudosection results (Fig. 10b).

The peak assemblage (Coe + Phe + Grt_R + Ky + Jd + Rt) is modelled by a large penta-variant field at T > 530°C and P > 25 kbar. Although garnet ($Sps_{1.7}Prp_{26}Grs_{3.5}Alm_{68}$) compositional isopleths are far apart, their intersection with phengite (Si = 3.45-3.49 a.p.f.u.) isopleths allows constraining peak P-T conditions at 660-730°C and 38-43 kbar (Fig. 10c), consistent with the peak P-T conditions proposed in previous papers and based on other lithologies (*i.e.*, pyrope-bearing whiteschists, eclogites, marbles; see review in Ferrando *et al.*, 2017). The AvPT approach applied on the peak assemblage did not converge to a result, because its variance is too high to define enough reactions.

5.4 Sample DM1504 (RSU)

The observed prograde and peak assemblage (Qz + Phe + Grt + Cld + Gln + Jd + Lws? + Rt) is modelled by a large quadri-variant field at 450-540°C, 19-25 kbar. The modelled garnet, chloritoid and phengite compositional isopleths intersect within this field and constrain prograde and peak P-T conditions as follows: (i) early prograde conditions are constrained at 490-510°C, 20-23 kbar using the compositions of garnet core ($Sps_9Prp_{8.5}Grs_{16}Alm_{67}$), of its chloritoid inclusions (X_{Mg}=0.20) and of phengite (Si=3.31-3.43 a.p.f.u.) (Fig. 11a); (ii) late prograde conditions are constrained at 500-520°C, 20-24 kbar using the compositions of garnet mantle ($Sps_6Prp_{9.5}Grs_{20}Alm_{64}$), of its chloritoid inclusions (X_{Mg}=0.22) and of phengite (Si=3.31-3.43 a.p.f.u.) (Fig. 11b); (iii) peak conditions are estimated at 510-525°C, 20-23 kbar using the compositions of garnet rim ($Sps_{4.5}Prp_9Grs_{18.5}Alm_{68}$), its chloritoid inclusions (X_{Mg}=0.24) and phengite (Si=3.31-3.43 a.p.f.u.) (Fig. 11c). The AvPT approach applied to four different sets of mineral compositions gives peak conditions of 495 ± 8 °C, 20.3 ± 0.6 kbar (Table 2), consistent with pseudosection results (Fig. 11c).

5.5 Sample DM1565 (DSU)

(Alpine) peak P-T conditions for this sample were estimated using the AvPT approach, applied to three different sets of mineral compositions. Although not observed in the sample, lawsonite was included in the peak assemblage, allowing to consider the reactions involving grossular, which are relevant because garnet

is relatively enriched in this component. This strategy is supported by the fact that other metapelites from the same unit show unambiguous evidence for the occurrence of lawsonite in the peak assemblage (Nosenzo, 2018). The AvPT results point to peak P-T conditions of 452 ± 8 °C, 17.2 ± 0.4 kbar (Table 2).

6. Discussion

6.1 New constraints on the prograde evolution of the tectonic units in the southern DMM

6.1.1 Prograde evolution of the HP units bounding the UHP BIU

The prograde P-T evolution inferred for the four units bounding the UHP BIU is summarized below:

- The PU experienced a prograde evolution starting in the lawsonite-blueschist facies and reaching peak conditions in the eclogite-facies (500-515°C, 20-23 kbar; Fig. 12a). Peak-T conditions are similar to those estimated by Avigad *et al*. (2003) (*i.e*., 530 °C) using multi-equilibrium thermobarometry applied on garnet-bearing metapelites from the same structural position. However, peak-P conditions are significantly higher than the 14-16 kbar estimated by the same authors (Fig. 12a).
- The P-T prograde path inferred for the SCU and RSU is remarkably similar to that constrained for the PU, with eclogite-facies peak P-T conditions at 500-520°C, 20-24 kbar (Fig. 12b, d). The estimated peak-P conditions are significantly higher than those (500-550°C, 15 kbar) constrained by Chopin *et al*. (1991) and Compagnoni & Rolfo (2003), whereas peak-T are in agreement with literature data (Fig. 12b, d).
- In contrast to the other units, the DSU did not experience eclogitic metamorphism. Estimated peak conditions (450-470 °C, 17-18 kbar) point to lawsonite-blueschist facies conditions (Fig. 12e); peak-T are similar to those reported by Chopin *et al*. (1991) (500°C, 10-12 kbar), but pressures are significantly higher (Fig. 12e).

Overall, our new data for the HP units bounding the UHP one substantially confirm peak-T already estimated more than 25 years ago, but point to a significant increase of peak-P estimates (ΔP = 5-10 kbar). This is the same trend already followed in the definition of peak P-T conditions for the UHP BIU, that were initially estimated to be at about 30 kbar (*e.g*., Chopin *et al*., 1991; Compagnoni *et al*., 1995) and progressively increased (35 kbar: *e.g*., Compagnoni & Rolfo, 2003) up to 40-43 kbar (*e.g*., Hermann, 2003; Castelli *et al*., 2007; Groppo *et al*., 2007a; Ferrando *et al*., 2009, 2017), in parallel with the progressive improvement of thermodynamic modeling approaches that extended the limits of conventional thermobarometry.

6.1.2 A revised prograde P-T path for the UHP BIU

Peak P-T conditions (730°C, 40-43 kbar) and retrograde evolution of the UHP BIU are now very well defined and were constrained in the last decades through detailed petrological studies on a great variety of lithologies, among them pyrope-bearing whiteschists (Schertl *et al*., 1991; Hermann, 2003; Ferrando *et al*., 2009; Gauthiez-Putallaz *et al*., 2016), eclogites (Nowlan *et al*., 2000; Di Vincenzo *et al*., 2006; Groppo *et al*., 2007a), marbles and calc-silicate rocks (Rubatto & Hermann, 2001; Ferraris *et al*., 2005; Di Vincenzo *et al*., 2006; Castelli *et al*., 2007). Garnet-bearing metapelites have never been used to constrain the BIU peak P-T conditions and have only been marginally used to constrain its retrograde evolution (Groppo *et al*., 2006). This is due to the fact that the highly variant assemblage (*i.e*., Coe + Phe + Grt + Ky + Jd) stable at UHP conditions is not suitable for application of conventional thermobarometry. Conversely, metapelites have been already used to constrain the early prograde evolution of the BIU, thanks to the preservation of abundant prograde inclusions in the core of porphyroblastic garnets. Chopin *et al*. (1991) and Michard *et al*. (1993) described a garnet-bearing phengitic micaschist (sample DM8412) very similar to our sample DM1281. Both their and our garnet porphyroblasts are, in turn, remarkably similar to the cores of the “superzoned” garnets described by Compagnoni & Hirajima (2001) (sample DM880). Chopin *et al*. (1991) and Compagnoni

& Hirajima (2001) interpreted the coexistence of chloritoid, kyanite, staurolite and chlorite in the polymineralic inclusions hosted within garnet cores as evidence that the BIU prograde trajectory passed close to the invariant point involving Cld + Ky + St + Chl, located around 600°C, 15 kbar. This was considered as a pinning point for the BIU prograde path for more than 25 years, resulting in a steep prograde trajectory located at temperatures significantly higher than the peak-T conditions estimated at that time for the adjacent units.

Our study unambiguously demonstrates that staurolite in the polymineralic inclusions hosted within garnet core and mantle has a retrograde nature, growing at the interface between garnet and kyanite, the latter mineral preserving a rounded/corroded shape (Fig. 4e). We suggest that staurolite grew during the retrograde evolution through a reaction that involved garnet, kyanite and chlorite as reactants. The aqueous fluid needed to trigger the reaction would not have been necessarily introduced from outside through fractures, but it could derive from the breakdown of chlorite associated with kyanite in the polymineralic inclusion (*i.e*., internally-derived fluid). Reaction modelling by the least square method (freeware application available on demand; Godard, 2009) applied to the composition of garnet core/mantle, chlorite, kyanite and staurolite yielded balanced reactions of this type: Chl + Ky + Grt = St (details are given in Table SM8), accounting for the retrograde formation of staurolite in a closed system, *i.e.* the polymineralic inclusion. The above-mentioned reaction is predicted to occur in the KFMASH system at about 600-650 °C, 13-15 kbar (White *et al*., 2014), and it would have been therefore intersected during the retrograde evolution of the BIU (Fig. 12c). It is worth noting that the growth of retrograde staurolite was already observed in the matrix of a garnet-bearing metapelite from the BIU, and was constrained exactly at these P-T conditions (Groppo *et al*., 2006).

The new interpretation of the nature of staurolite occurring in the polymineralic inclusions hosted in the BIU garnet porphyroblasts has important consequences for the definition of the BIU prograde P-T path. The results of thermodynamic modeling and AvPT tightly constrain the growth of garnet core at 520-540°C, 16-23 kbar, *i.e*., at significantly lower T and higher P than previously estimated, and at P-T conditions close to the peak P-T conditions of the adjacent units. Moreover, the growth of garnet mantle is modeled at UHP conditions, consistent with the occurrence of pseudomorphs after coesite included in the mantle domain. The whole prograde evolution of the BIU is thus significantly different from that previously assumed; it does not follow a regularly steep P/T gradient, but it is rather characterized by: (i) an early prograde evolution along a moderately steep P/T gradient, similar to that followed by the adjacent HP units; (ii) an intermediate steep, almost isothermal, pressure increase, and (iii) a late prograde temperature increase along a moderately steep P/T gradient, still at increasing pressure.

6.2 Implications for the geodynamic interpretation of the southern DMM

An in-depth discussion of the geodynamic processes responsible for the architecture of the southern DMM is beyond the aim of this paper. However, the following conclusions are worth noting and could represent new constraints for future investigations:

(1) the PU experienced eclogite-facies metamorphism under peak P-T conditions very similar to those registered by the SCU and RSU (500-520°C, 20-24 kbar). Moreover, the PU, SCU and RSU units followed the same prograde path, along a medium T/P gradient of about 12°C $kbar^{-1}$, suggesting similar burial mechanisms. The similarity of the peak P-T conditions experienced by the PU and SCU, combined with the fact that the PU sample was collected from an outcrop located very close to the contact with the BIU (Fig. 1), could potentially raise the doubt that the two samples actually belong to the same unit (*i.e*., SCU). The contact between the PU and overlying units (either SCU or BIU) has been located thanks to the abrupt occurrence, moving downward in the DMM nappe stack, of abundant graphitic micaschists with quartzite intercalations (see Fig.1). These micaschists have never been described within the other units (either

SCU, BIU or RSU) and, in turn, have been considered diagnostic of the former PU (e.g., Vialon, 1966; Chopin *et al*., 1991; Avigad *et al*., 2003). Following this criterion, sample DM1485 has been attributed to the PU. Our results thus highlight that, in the investigated area, the PU does not correspond to a blueschist unit, as previously described (Avigad *et al*., 2003), and therefore the actual occurrence of a blueschist unit stacked below an eclogitic ones has to be restricted to northernmost sectors of the DMM (*i.e*., the Brianconnais-like tectonic window in the Pinerolo area; *e.g*., Manzotti *et al.,* 2016).

(2) the UHP BIU seems to have followed an early prograde evolution similar to that of the other eclogitic units of the southern DMM tectonic "sandwich". The attainment of UHP peak conditions occurred through an earlier almost isothermal increase in pressure (ΔP=8-10 kbar) along a significantly lower T/P gradient (ca. 3°C kbar^{-1}) and a later increase in temperature (ΔT=150-170 °C) along a medium T/P gradient (ca. 15°C kbar^{-1}). Our results suggest that UHP metamorphism was not the result of a single, homogeneous, process, but rather the product of a two-step process. Further geochronological studies are needed in order to test if the UHP BIU shared a synchronous prograde evolution with the adjacent eclogitic units.

(3) the DSU is the only unit of the southern DMM tectonic "sandwich" that, according to our results, did not experience eclogite-facies metamorphism. It is worth noting that, on the field, the DSU is separated from the eclogitic units by a hundreds of metres thick shear zone (tectonic mélange *sensu* Festa *et al*., 2019), which includes slices of meta-ophiolite (Valmala Shear Zone: Nosenzo, 2018). The detailed description and interpretation of this shear zone is beyond the aim of this paper and further studies are necessary to understand its role in decoupling the southern DMM during subduction and/or in driving exhumation of related (U)HP units.

Acknowledgements

Roberto Compagnoni introduced most of us to the fascinating southern Dora-Maira Massif and to the beauty and challenges of metamorphic petrology. R. Compagnoni, R. Turello and T. Hirajima collected sample DM1281 studied in this paper. Two anonymous reviewers provided constructive comments which significantly improved the manuscript; the Guest Editor is warmly thanked for its several constructive remarks and its meticulous editorial handling. This research was funded by University of Torino, Ricerca Locale, ex-60% 2016, 2017 funds: FERS_RILO_17_01 (SF), FESA_RILO_17_01 (AF), GROC_RILO_17_01 (CG), ROLF_RILO_16_01 (FR), and by the Italian Ministry of University and Research, PRIN 2015: 2015EC9PJ5 (GB).

References

Avigad, D., Chopin, C., Le Bayon R. (2003): Thrusting and extension in the southern Dora-Maira ultra-high pressure massif (Western Alps): view from below the coesite-bearing unit. *J. Geol.*, **111**, 57–70.

Balestro, G., Cadoppi, P., Di Martino, L., Sacchi, R. (1995): Il settore meridionale del Massiccio Dora-Maira (Valli Maira e Varaita): inquadramento, carta geologica e guida a un'escursione. Rapporti Alpi-Appennino e guida alle escursioni. *Accademia Nazionale delle Scienze*, **14**, 501–529.

Balestro, G., Festa, A., Borghi, A., Castelli, D., Gattiglio, M., Tartarotti, P. (2018): Role of Late Jurassic intra-oceanic structural inheritance in the Alpine tectonic evolution of the Monviso meta-ophiolite Complex (Western Alps). *Geol. Magaz.*, **155** (2), 233-249.

Biino, G. & Compagnoni R. (1992): Very high pressure metamorphism of the Brossasco coronite metagranite, southern Dora-Maira Massif, Western Alps. *Schweiz. Mineral. Petrogr. Mitt*., **72**, 347–363.

Botta, S. (2015): Studio geologico-petrografico dell'Unità di Rocca Solei, Massiccio Dora-Maira meridionale (Alpi Occidentali). Unpublished MSc Thesis, Univ. Torino, Italy, 245 pp.

Burov, E., Francois, T., Yamato, P., Wolf, S. (2014): Mechanisms of continental subduction and exhumation of HP and UHP rocks. *Gondw. Res*., **25**, 464–493.

Butler, J.P., Beaumont, C., Jamieson, R.A. (2013): The Alps 1: a working geodynamic model for burial and exhumation of (ultra)high-pressure rocks in Alpine-type orogens. *Earth Planet. Sci. Lett*., **377–378**, 114–131.

Castelli, D., Rolfo, F., Groppo, C., Compagnoni, R. (2007): Impure marbles from the UHP Brossasco-Isasca Unit (Dora-Maira Massif, Western Alps): evidence for Alpine equilibration in the diamond stability field and evaluation of the X(CO_2) fluid evolution. J*. metamorphic Geol*., **25**, 587–603.

Chemenda, A.I., Mattauer, M., Mattavieille, J., Bokun, A.N. (1995): A mechanism for syn-collisional rock exhumation and associated normal faulting: results from physical modelling. *Earth Planet. Sci. Lett*. **132**, 225–232.

Chopin, C. (1984): Coesite and pure pyrope in high-grade blueschists of the Western Alps: a first record and some consequences. *Contrib. Mineral. Petrol*., **86**, 107–118.

— (2003): Ultrahigh-pressure metamorphism: tracing continental crust into the mantle. *Earth Planet. Sci. Lett*., **212**, 1–14.

Chopin, C., Henry, C. Michard, A. (1991): Geology and petrology of the coesite-bearing terrain, Dora Maira Massif, Western Alps. *Eur. J. Mineral*., **3**, 263–291.

Compagnoni, R. & Hirajima, T. (2001): Superzoned garnets in the coesite-bearing Brossasco-Isasca Unit, Dora-Maira massif, western Alps, and the origin of the whiteschists. *Lithos*, **57**, 219–236.

Compagnoni, R. & Rolfo, F. (1999): Characteristics of UHP pelites, gneisses and other unusual rocks. *International Geology Review,* **41**, 552-570.

—, — (2003): Ultrahigh-pressure units in the Western Alps. *in*: "Ultrahigh-pressure metamorphism", D.A. Carswell & R. Compagnoni, eds, *EMU Notes in Mineralogy*, **5**, 13–49.

Compagnoni, R., Hirajima, T., Chopin, C. (1995): Ultra-high pressure metamorphic rocks in the Western Alps. *in*: "Ultrahigh Pressure Metamorphism", R.G. Coleman & X. Wang, eds., Cambridge University Press, 206–243.

Compagnoni, R., Rolfo, F., Groppo, C., Hirajima, T., Turello R. (2004): Mapping of Alpine rocks characterized by "HP" to "UHP" metamorphic overprint in the southern Dora-Maira Massif (Western Alps). *in*: "Mapping Geology in Italy", G. Pasquare & C. Venturini, eds., APAT, Dipartimento Difesa del Suolo, Servizio Geologico d'Italia, Roma 2004 (2006), **Map 34**, 287–294, Printed by S.EL.CA., Firenze.

Compagnoni, R., Rolfo, F., Groppo, C., Hirajima, T., Turello R. (2012): Geologic map of the UHP Brossasco-Isasca Unit (Western Alps). *J. Maps*, **8/4**, 465–472.

667 Connolly (1990): Multivariable phase diagrams: an algorithm based on generalized thermodynamics. *Am. J.*
668 *Sci*., **290**, 666–718.
669 — (2005): Computation of phase equilibria by linear programming: A tool for geodynamic modeling and its
670 application to subduction zone decarbonation. *Earth Planet. Sci. Lett*., **236**, 524–541.
671 — (2009): The geodynamic equation of state: what and how. *Geochem. Geophys. Geosyst*., **10**, Q10014.
672 Cossio, R., Borghi, A., Ruffini, R. (2002): Quantitative modal determination of geological samples based on X-
673 ray multielemental map acquisition. *Microsc. Microanal*., **8**, 139–149.
674 Di Vincenzo, G., Tonarini, S., Lombardo, B., Castelli, D., Ottolini, L. (2006): Comparison of ^{40}Ar-^{39}Ar and Rb-Sr
675 data on phengites from the UHP Brossasco-Isasca Unit (Dora Maira Massif, Italy): Implications for dating
676 white mica. *J. Petrol*., **47**, 1439–1465.
677 Ferrando, S., Frezzotti, M.L., Petrelli, M., Compagnoni, R. (2009): Metasomatism of continental crust during
678 subduction: the UHP white schists from the southern Dora-Maira Massif (Italian Western Alps). *J.*
679 *metamorphic Geol*., **27**, 739–756.
680 Ferrando, S., Groppo, C., Frezzotti, M.L., Castelli, D., Proyer, A. (2017): Dissolving dolomite in a stable UHP
681 mineral assemblage: evidence from Cal-Dol marbles of the Dora-Maira Massif (Italian Western Alps). *Am.*
682 *Mineral*., **102**, 42–-60.
683 Ferraris, C., Castelli, D., Lombardo, B. (2005): SEM/TEM-AEM characterization of micro- and nano-scale
684 zonation in phengite from a UHP Dora-Maira marble: Petrologic significance of armoured Si-rich domains.
685 *Eur. J. Mineral*., **17**, 453–464.
686 Festa, A., Pini, G.A., Ogata, K., Dilek, Y. (2019): Diagnostic features and field-criteria in recognition of tectonic,
687 sedimentary and diapiric mélanges in orogenic belts and exhumed subduction-accretion complexes.
688 *Gondw. Res.*, **online version**, https://doi.org/10.1016/j.gr.2019.01.003.
689 Ford, M., Duchéne, S., Gasquet, D., Vanderhaeghe, O. (2006): Two-phase orogenic convergence in the
690 external and internal SW Alps. *J. Geol. Soc*., **163**, 815–826.
691 Fuhrman, M.L. & Lindsley, D.H. (1988): Ternary-Feldspar Modeling and Thermometry. *Am. Mineral*., **73**, 201–
692 215.
693 Gauthiez-Putallaz, L., Rubatto, D., Hermann, J. (2016): Dating prograde fluid pulses during subduction by in
694 situ U–Pb and oxygen isotope analysis. *Contrib. Mineral. Petrol.*, **171**, article 15, 20 pp.
695 Gerya, T. (2015): Tectonic overpressure and underpressure in lithospheric tectonics and metamorphism. *J.*
696 *metamorphic Geol*., **33**, 785–800.
697 Gerya, T. & Stöckhert, B. (2006): Two-dimensional numerical modeling of tectonic and metamorphic histories
698 at active continental margins. *Int. J. Earth Sci. (Geol. Rundsch*.), **95**, 250–274.
699 Godard, G. (2009): Two orogenic cycles in eclogite-facies gneisses of the Southern Armorican Massif (France).
700 Eur. J. Mineral., **21**, 1173–1190.
701 Green, E.C.R., Holland, T.J.B., Powell, R. (2007): An order–disorder model for omphacitic pyroxenes in the
702 system jadeite–diopside–hedenbergite–acmite, with applications to eclogite rocks. *Am. Mineral*., **92**,
703 1181–1189.
704 Green, E.C.R., White, R.W., Diener, J.F.A., Powell, R., Holland, T.J.B., Palin, R.M. (2016): Activity–composition
705 relations for the calculation of partial melting equilibria in metabasic rocks. *J. metamorphic Geol.*, **34**, 845–
706 869.
707 Groppo, C. (2002): Studio geologico-petrografico della terminazione nord-occidentale dell'Unita Brossasco-
708 Isasca in facies eclogitica a coesite, Massiccio Dora-Maira (Alpi Occidentali). Unpublished M.Sc. Thesis,
709 Univ. Torino, Italy, 175 pp.
710 Groppo, C., Castelli, D., Compagnoni, R. (2006): Late chloritoid-staurolite assemblage in a garnet-kyanite
711 bearing metapelite from the UHP Brossasco-Isasca Unit (Dora-Maira Massif, Western Alps): new
712 petrological constraints for a portion of the P-T decompressional path. *in*: "Ultrahigh-pressure

713 metamorphism: Deep continental subduction", B.H. Hacker, W.C. McClelland & J.G. Liou J.G., eds., GSA
714 Special Paper, **403**, 127–138.
715 Groppo, C., Castelli, D., Rolfo, F. (2007b): HT, Pre-Alpine relics in a spinel-bearing dolomite marble from the
716 UHP Brossasco-Isasca Unit (Dora-Maira Massif, western Alps). *Per. Mineral*., **76**, 155–168.
717 Groppo, C., Lombardo, B., Castelli, D., Compagnoni, R. (2007a): Exhumation history of the UHPM Brossasco-
718 Isasca Unit, Dora-Maira Massif, as inferred from a phengite-amphibole eclogite. *Int. Geol. Rev*., **49**, 142–
719 168.
720 Guiraud, M., Holland, T.J.B., Powell R. (1990): Calculated mineral equilibria in the greenschist-blueschist-
721 eclogite facies in Na_2O-FeO-MgO-Al_2O_3-SiO_2-H_2O: methods, results and geological applications. *Contrib.*
722 *Mineral. Petrol.*, **104**, 85–98.
723 Henry, C. (1990): L'unité à coesite du massif Dora-Maira dans son cadre pétrologique et structurale (Alpes
724 Occidentales, Italie). Thése Doctorat., Université Paris 6, 149 pp.
725 Henry, C., Michard, A., Chopin, C. (1993) : Geometry and structural evolution of ultra-high pressure and high
726 pressure rocks from the Dora-Maira massif, western Alps, Italy. *J. Struct. Geol.*, **15**, 965–981.
727 Hermann, J. (2003): Experimental evidence for diamond-facies metamorphism in the Dora-Maira massif.
728 *Lithos*, **70**, 163–182.
729 Holland, T.J.B. & Powell, R. (1998): An internally consistent thermodynamic dataset for phases of petrological
730 interest. J. *metamorphic Geol*., **16**, 309–343.
731 —, — (2011): An improved and extended internally consistent thermodynamic dataset for phases of
732 petrological interest, involving a new equation of state for solids. *J. metamorphic Geol*., **29**, 333–383.
733 Lardeaux, J., Schwartz, S., Tricart, P., Paul, A., Guillot, S., Béthoux, N., Masson, F. (2006): A crustal-scale cross-
734 section of the south-western Alps combining geophysical and geological imagery. *Terra Nova*, **18** (6), 412–
735 422.
736 Li, Z., Gerya, T.V., Burg, J.P. (2010). Influence of tectonic overpressure on P-T paths of HP–UHP rocks in
737 continental collision zones: thermomechanical modelling. *J. metamorphic Geol.*, **28**, 227–247.
738 Liou, J.G. & Zhang, R.Y. (2002): Ultrahigh-pressure metamorphic rocks. Ency Phys Sci Tech (Third Edition). 17,
739 Academia Press, 227–244.
740 Manzotti, P., Pitra, P., Langlade, J., Ballèvre, M. (2015): Constraining P-T conditions during thrusting of a
741 higher pressure unit over a lower pressure one (Gran Paradiso, Western Alps). *J. metamorphic Geol.*, **33**,
742 981–1002.
743 Manzotti, P., Ballèvre, M., Poujol, M. (2016): Detrital zircon geochronology in the Dora Maira and Zone
744 Houillère: A record of sediment travel paths in the Carboniferous. *Terra Nova*, *28*, 279–288.
745 Matsumoto, N. & Hirajima, T. (2000): Garnet in pelitic schists from a quartz-eclogite unit of the southern
746 Dora-Maira massif, Western Alps. *Schweiz. Mineral. Petrol. Mitt*., **80**, 53–62.
747 Manzotti, P., Bosse, V., Pitra, P., Robyr, M., Schiavi, F., Ballèvre, M. (2018): Exhumation rates in the Gran
748 Paradiso (Western Alps) constrained by in situ U-Th-Pb dating of accessory phases (monazite, allanite and
749 xenotime). *Contrib. Mineral. Petrol.*, **173**, 24.
750 Michard, A., Chopin, C., Henry, C. (1993): Compression versus extension in the exhumation of the Dora-Maira
751 coesite-bearing unit, Western Alps. *Tectonophysics*, **221**, 173–193.
752 Michard, A., Henry, C., Chopin, C. (1995): Structures in UHPM rocks: a case study from the Alps. *in*: "Ultrahigh
753 Pressure Metamorphism", R.G. Coleman & X. Wang, eds., Cambridge University Press, 132-158.
754 Michard, A., Goffe, B., Chopin, C., Henry, C. (1996): Did the Western Alps develop through an Oman-type
755 stage? The geotectonic setting of high-pressure metamorphism in two contrasting Tethyan transects. *Ecl.*
756 *Geol. Helv.*, **89**, 43– 80.
757 Nosenzo (2018): Studio geologico-strutturale e metamorfico del massiccio Dora-Maira meridionale in
758 Valmala (Valle Varaita, Alpi Occidentali). Unpublished M.Sc. Thesis, Univ. Torino, Italy, 187 pp.

759 Nowlan, E.U., Schertl, H.P., Schreyer, W. (2000): Garnet–omphacite–phengite thermobarometry of eclogites
760 from the coesite-bearing unit of the southern Dora-Maira Massif, Western Alps. *Lithos*, **52**, 197–214.
761 Pouchou, J.L. & Pichoir, F. (1988): Determination of mass absorption coefficients for soft X-rays by use of the
762 electron microprobe. Microbeam Analysis. San Francisco Press, San Francisco, 319–324 p.
763 Powell, R. & Holland, T.J.B. (1994): Optimal geothermometry and geobarometry. *Am. Mineral*., **79**, 120–133.
764 Proyer, A. (2003): Metamorphism of pelites in NKFMASH - a new petrogenetic grid with implications for the
765 preservation of high pressure mineral assemblages during exhumation. *J. metamorphic Geol*., **21**, 493–
766 509.
767 Reuber, G., Kaus, B.J.P., Schmalholz, S.M., White, R.W. (2016): Nonlithostatic pressure during subduction and
768 collision and the formation of (ultra)high-pressure rocks. *Geology*, **44**, 343–346.
769 Rubatto, D. & Hermann, J. (2001): Exhumation as fast as subduction? *Geology*, **29**, 3–6.
770 Sandrone R., Cadoppi P., Sacchi R., Vialon P. (1993): The Dora-Maira Massif. *in*: "Pre-Mesozoic Geology in the
771 Alps", J.F. von Raumer & F.Neubauer, eds., Springer-Verlag, 317-325.
772 Schenker, F.L., Schmalholz, S.M., Moulas, E., Pleuger, J., Baumgartner, L.P., Podladchikov, Y., Vrijmoed, J.,
773 Buchs, N., Müntener O. (2015): Current challenges for explaining (ultra)high-pressure tectonism in the
774 Pennine domain of the Central and Western Alps. *J. metamorphic Geol.,* **33**, 869–886.
775 Schertl, H.P. & O'Brien, P.J. (2013): Continental Crust at Mantle Depths: Key Minerals and Microstructures.
776 *Elements*, **9**, 261–266.
777 Schertl, H.P., Schreyer, W., Chopin, C. (1991): The pyrope-coesite rocks and their country rocks at Parigi, Dora
778 Maira Massif, Western Alps: detailed petrography, mineral chemistry and P-T path. *Contrib. Mineral.*
779 *Petrol*., **108**, 1–21.
780 Schmalholz, S.M. & Duretz, T. (2015): Shear zone and nappe formation by thermal softening, related stress
781 and temperature evolution, and application to the Alps *J. metamorphic Geol.,* **33**, 887–908.
782 Schmalholz, S.M., Duretz, T., Schenker, F.L., Podladchikov, Y.Y. (2014): Kinematics and dynamics of tectonic
783 nappes: 2-D numerical modelling and implications for high and ultrahigh pressure tectonism in the
784 Western Alps. *Tectonophysics*, **631**, 160–175.
785 Sharp, Z.D., Essene, E.J., Hunziker, J.C. (1993): Stable isotope geochemistry and phase equilibria of coesite-
786 bearing whiteschists, Dora Maira Massif, western Alps. *Contrib. Mineral. Petrol*., **114**, 1–12.
787 Smith, D.C. (1984): Coesite in clinopyroxene in the Caledonides and its implications for geodynamics. *Nature*,
788 **310**, 641–644.
789 Smye, A.J., Greenwood, L.V., Holland, T.J.B. (2010): Garnet–chloritoid–kyanite assemblages: eclogite facies
790 indicators of subduction constraints in orogenic belts. *J. metamorphic Geol.,* **28**, 753–768.
791 Solarino, S., Malusà, M.G., Eva, E, Guillot, S., Paul, A., Schwartz, S., Zhao, L., Aubert, C., Dumont, T., Pondrelli,
792 S., Salimbeni, S., Wang, Q., Xu, X., Zheng, T., Zhu, R. (2018): Mantle wedge exhumation beneath the Dora-
793 Maira (U)HP dome unravelled by local earthquake tomography (Western Alps). *Lithos*, **296–299**, 623–636.
794 Stöckhert, B. & Gerya, T.V. (2005): Pre-collisional high pressure metamorphism and nappe tectonics at active
795 continental margins: a numerical simulation. *Terra Nova*, **17**, 102–110.
796 Turello, R. (1993): Studio geologico e petrografico dell'area tra Martiniana (Valle Po) e Brossasco (Valle
797 Varaita) - Massiccio Dora-Maira meridionale. Unpublished M.Sc. Thesis, Univ. Torino, Italy, 238 pp.
798 Vialon, P. (1966): Etude géologique du Massif Cristallin Dora-Maira, Alpes Cottiennes internes, Italie. PhD
799 Tesis, Univ. Grenoble, Travaux du Lab. Géol. Fac. Sci. Grenoble, Memoir 4, 193 pp
800 Wei, C.J. & Powell, R. (2004): Calculated phase relations in high-pressure metapelites in the system NKFMASH
801 (Na_2O-K_2O-FeO-MgO-Al_2O_3-SiO_2-H_2O). *J. Petrol*., **45**, 183–202.
802 —, — (2006): Calculated phase relations in the system NCKFMASH (Na_2O-CaO-K_2O-FeO-MgO-Al_2O_3-SiO_2-H_2O)
803 for high-pressure metapelites. *J. Petrol*., **47**, 385–408.

White, R.W., Powell, R., Holland, T.J.B., Johnson, T.E., Green, E.C.R. (2014): New mineral activity–composition relations for thermodynamic calculations in metapelitic systems. *J. metamorphic Geol*., **32**, 261–286.

Whitney, D.L. & Evans, B.W. (2010): Abbreviations for names of rock-forming minerals. *Am. Mineral.*, **95**, 185–187.

Yamato, P., Burov, E., Agard, P., Le Pourhiet, L., Jolivet, L. (2008): HP-UHP exhumation during slow continental subduction: self-consistent thermodynamically and thermomechanically coupled model with application to the Western Alps. *Earth Planet. Sci. Lett*., **271**, 63–74.

Figure captions

Fig. 1 – Simplified geological map (a) of the southern Dora-Maira Massif around the UHP Brossasco-Isasca Unit (modified from Compagnoni *et al*., 2012, and with unpublished data from Botta, 2015, and Nosenzo, 2018). Sample locations are shown by black stars both in the map and cross sections. The Polymetamorphic and Monometamorphic Complexes in the SCU, BIU, RSU and DSU refer to a Variscan amphibolite-facies metamorphic basement and to Permian igneous bodies, respectively, each of which reworked during Alpine metamorphism. The insets (b, c) show the location of the southern DMM in north-west Italy (b) and within a simplified tectonic sketch-map of the Western Alps (c).

Fig. 2 – Processed micro-XRF maps of the studied metapelites. For sample DM1565 (DSU), Grt_C and Grt_M refer to pre-Alpine Grt_1 porphyroblasts, whereas Alpine Grt_2 idioblasts in the matrix are reported as Grt_R. Dark-grey to black domains are holes in the thin sections (*i.e*., pixels not assigned to mineral phases).

Fig. 3 – Representative microstructures of samples DM1485 (a, b) and DM1667c (c-e) from the PU and SCU, respectively. Sample DM1485: (a) Garnet porphyroblast with a snow-ball structure including quartz and chloritoid. The plagioclase porphyroblasts in the matrix are related to retrogression. (b) Detail of chloritoid + phengite + paragonite polymineralic inclusion in garnet mantle. Sample DM1667c: (c) Detail of chloritoid included in garnet mantle, partially replaced by white mica. (d) Fine-grained epidote included in garnet mantle. (e) Box-shaped pseudomorph after lawsonite included in garnet rim, consisting of epidote + phengite + paragonite + chlorite. (a, b, c: Plane Polarized Light, PPL; d, e and insets in a, b; Crossed Polarized Light, XPL).

Fig. 4 – Representative microstructures of sample DM1281 from the BIU. (a) Zoned garnet porphyroblast, with a large core and mantle crowded with fine-grained inclusions, and a thin rim with few inclusions. The main foliation is defined by phengite. The inset shows a pseudomorph after coesite, consisting of polycrystalline quartz, included in garnet mantle. (b) Detail of a pluri-mm kyanite porphyroblast (Ky_1) enveloped by the main foliation. Small idioblasts of Ky_2 are in equilibrium with the S_m. (c) Pseudomorph after jadeite, consisting of a fine-grained aggregate of albite, pyrophyllite and paragonite. (d) Fine-grained polymineralic inclusions in garnet mantle. The inset shows a polymineralic inclusion in garnet core: note the equilibrium relations among chloritoid, chlorite and paragonite. (e) Details of polymineralic inclusions in garnet mantle, consisting of kyanite, staurolite, paragonite and chlorite. Staurolite systematically separates corroded/rounded kyanite grains from garnet, suggesting that its growth is related to a reaction between garnet and kyanite. (f, g) Pseudomorphs after glaucophane (f) and jadeite (g) included in garnet mantle, consisting of fine-grained aggregates of paragonite + muscovite ± biotite and albite + pyrophyllite + paragonite, respectively. (a, b, c, f, g: XPL; c, d: PPL; e and inset in d: Back Scattered Electron image, BSE).

Fig. 5 – Representative microstructures of samples DM1504 (a-c) and DM1565 (d-f) from the RSU and DSU, respectively. Sample DM1504: (a) Garnet porphyroblast with quartz and chloritoid inclusions, partially enveloped by the main foliation, defined by phengite and chloritoid. (b) Detail of the chloritoid inclusions in garnet core and mantle. The inset shows a very fine-grained polymineralic inclusion in garnet mantle, consisting of glaucophane and jadeite, partially replaced by albite, pyrophyllite and paragonite. (c) Tabular-shaped inclusion in garnet mantle, consisting of an aggregate of epidote + paragonite + quartz, possibly deriving from former lawsonite. Sample DM1565: (d) Large pre-Alpine garnet porphyroblasts (Grt_1) enveloped by the main foliation. (e) Top: small Alpine garnet idioblasts (Grt_2) in equilibrium with the main foliation defined by phengite; bottom: Grt_2 forming a discontinuous rim around Grt_1. (f) Large aggregate of

fine-grained chloritoid enveloped by the S_m and interpreted as a pseudomorph after pre-Alpine staurolite. (a, b, c, d, e: PPL; f and insets in a, d: XPL; inset in b: BSE).

Fig. 6 – Garnet compositions plotted in the Prp-Alm-(Grs+Sps) diagram. The zoning trend for each sample is highlighted by the arrow. Samples are grouped according to their bulk-composition (*i.e.*, Ca-poor vs. Ca-rich metapelites). For sample DM1565, only compositions of Alpine Grt_2 are plotted.

Fig. 7 – Potassic white mica compositions plotted in the Si vs. Fe^{2+} + Mg (a.p.f.u.) diagram. Compositions of micas defining the S_m are distinguished from those included in garnet and from the late flakes overgrowing the S_m. Samples are grouped according to their bulk-composition (*i.e.*, oxidized vs. not oxidized). The dashed line represents the ideal celadonitic substitution. Note that point analyses for samples DM1485 (PU), DM1667c (SCU) and DM1504 (RSU) plot slightly above the line of ideal celadonite substitution, thus suggesting that these white micas contain some Fe^{3+}.

Fig. 8 – P-T pseudosections modeled for sample DM1485 (PU) using the measured bulk-composition (a), and the effective bulk-compositions after fractionation of garnet core (b) and of garnet core + mantle (c). Dotted lines are Rt and Ilm -in/out curves; dashed line is the Qz/Coe transition. The black ellipses show the P-T conditions constrained for the growth of garnet core (a), mantle (b) and rim (c), based on the intersection of compositional isopleths, as indicated in each legend. Dark grey squares with dotted ellipses in (c) represent peak P-T conditions (with 1σ error) as defined by AvPT applied on four different sets of mineral compositions (see Table 2).

Fig. 9 – P-T pseudosections modeled for sample DM1667c (SCU). (a), (b), (c) and all the symbols as in Fig. 8.

Fig. 10 – P-T pseudosections modeled for sample DM1281 (BIU). (a), (b), (c) and all the symbols as in Fig. 8; the inset in (b) clarifies the mineral assemblages stable in the narrow fields modelled in the central part of the pseudosection. Note that the scale is different from that in Fig. 8, 9 and 11, that pseudosection in (c) has been calculated at $a H_2O$=0.4, and that AvPT data in (b) refer to late prograde P-T conditions.

Fig. 11 – P-T pseudosections modeled for sample DM1504 (RSU). (a), (b), (c) and all the symbols as in Fig. 8.

Fig. 12 – (a-e) P-T grids showing the prograde trajectories for the Pinerolo Unit (a), San Chiaffredo Unit (b), Brossasco-Isasca Unit (c), Rocca Solei Unit (d) and Dronero-Sampeyre Unit (e) as inferred in this study, compared to peak P-T conditions derived from the literature (PU: Avigad *et al.*, 2003; SCU: Compagnoni & Rolfo, 2003; BIU: Ferrando *et al.*, 2017 and references therein; RSU: Chopin *et al.*, 1991; Matsumoto & Hirajima, 2000; DSU: Chopin *et al.*, 1991). For the BIU, the prograde and retrograde P-T path inferred from the literature is also reported. KFMASH reactions relevant for the discussion are reported in (c) (from White *et al.*, 2014). Note that the BIU retrograde trajectory crosses the Grt + Ky + Chl = St reaction (see Section 6.**1.**2 for further discussion). (f) Comparison of the prograde P-T trajectories inferred for all the studied units: note that the early prograde path of the BIU is similar to the P-T trajectory of the other units. Metamorphic facies are from Liou & Zhang, 2002. The chloritoid stability field, as derived from pseudosections of Fig. 8-11, is reported in greenish-blue.

Fig. 1

Click here to access/download;Figure;Fig1.tif

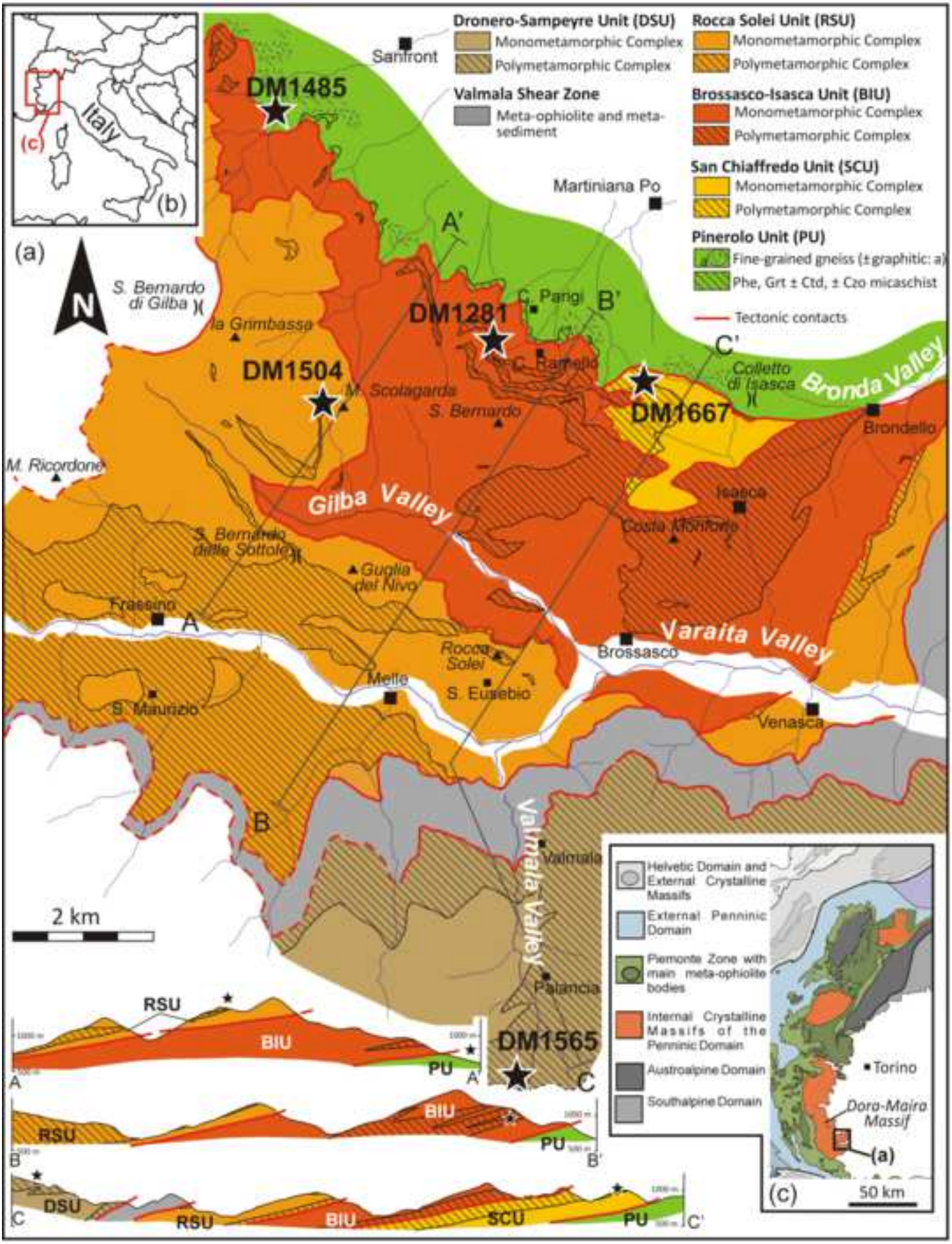

Fig. 2

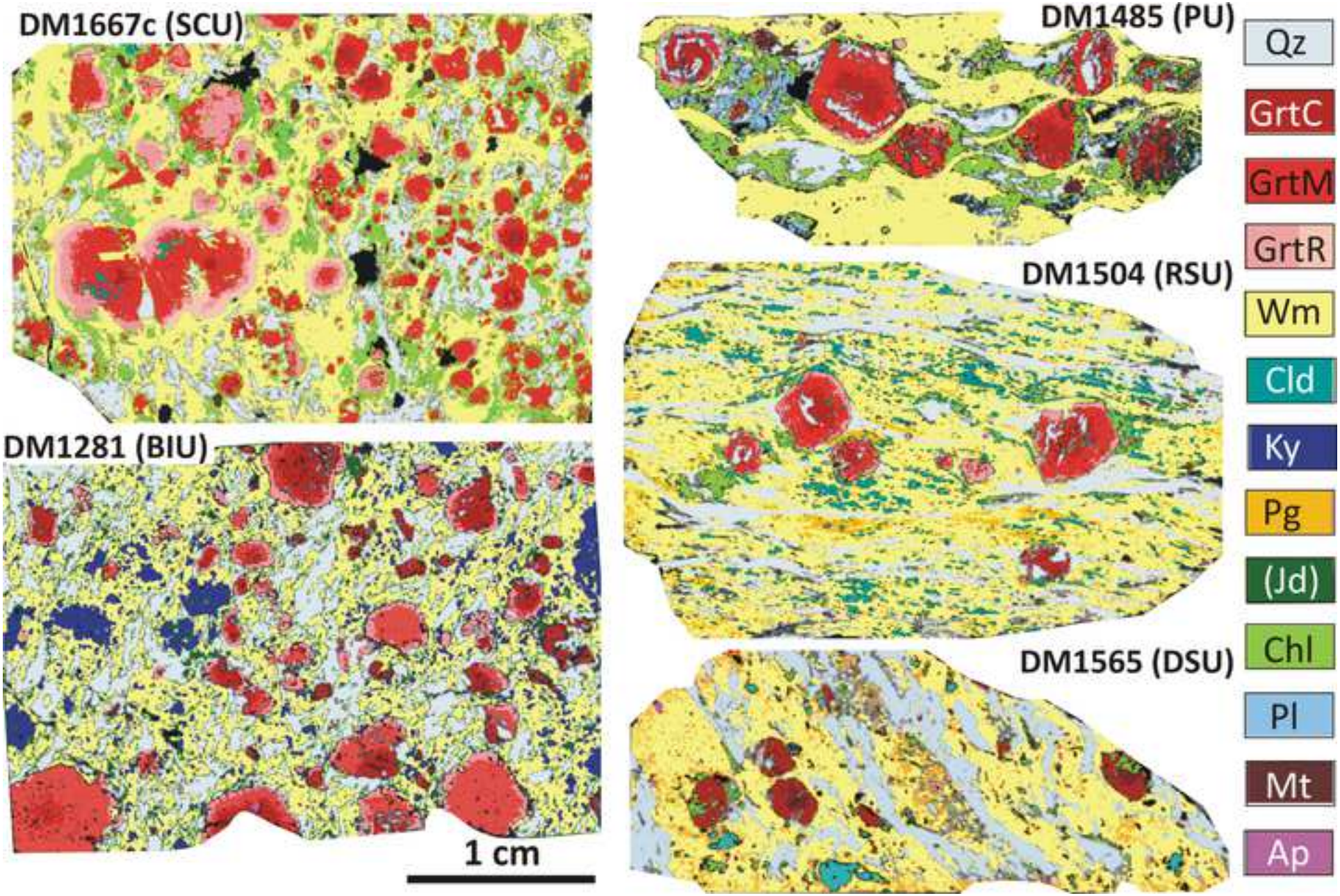

Fig. 3

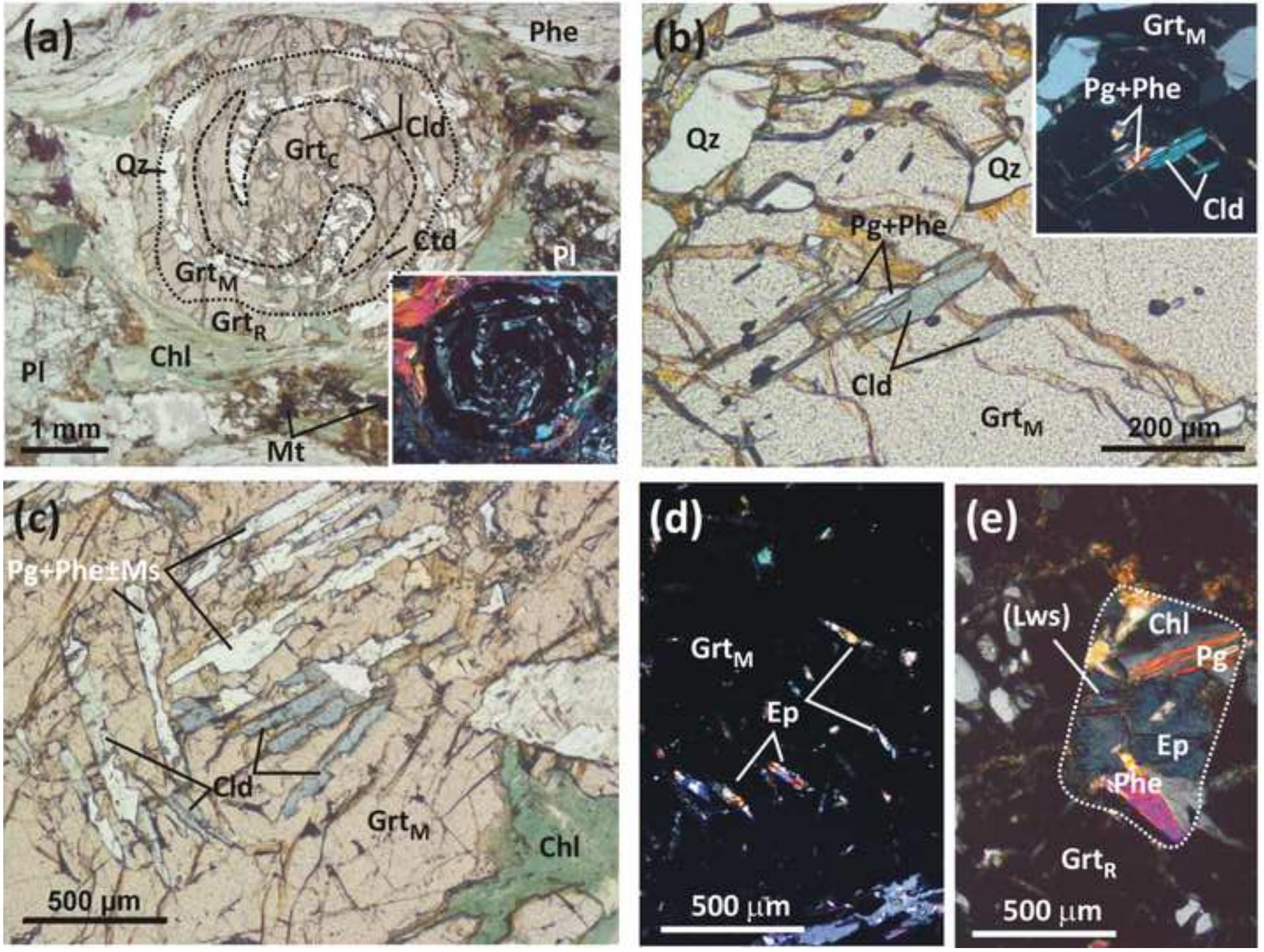

Fig. 4

Click here to access/download;Figure;Fig4.tif

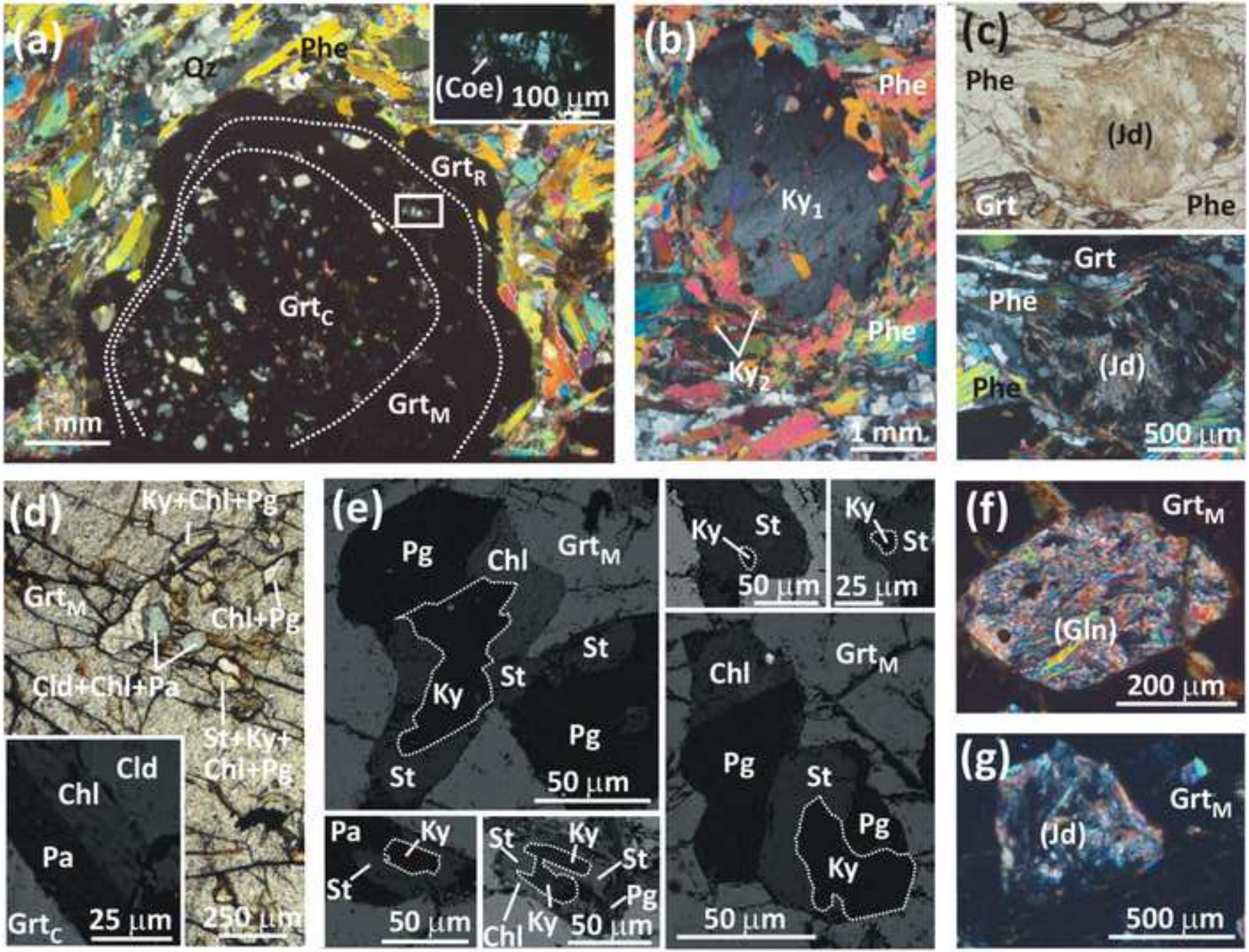

Fig. 5

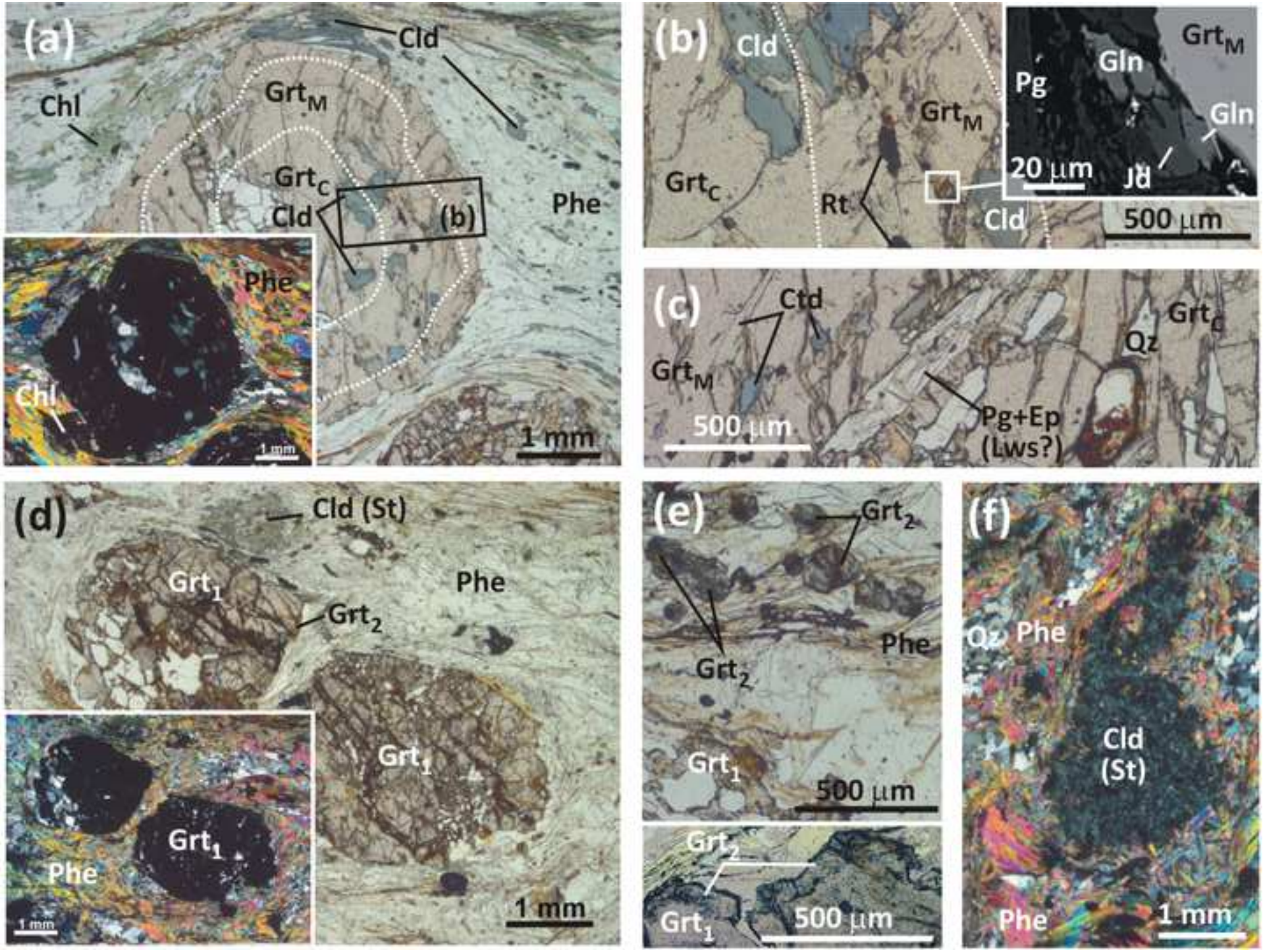

Fig. 6

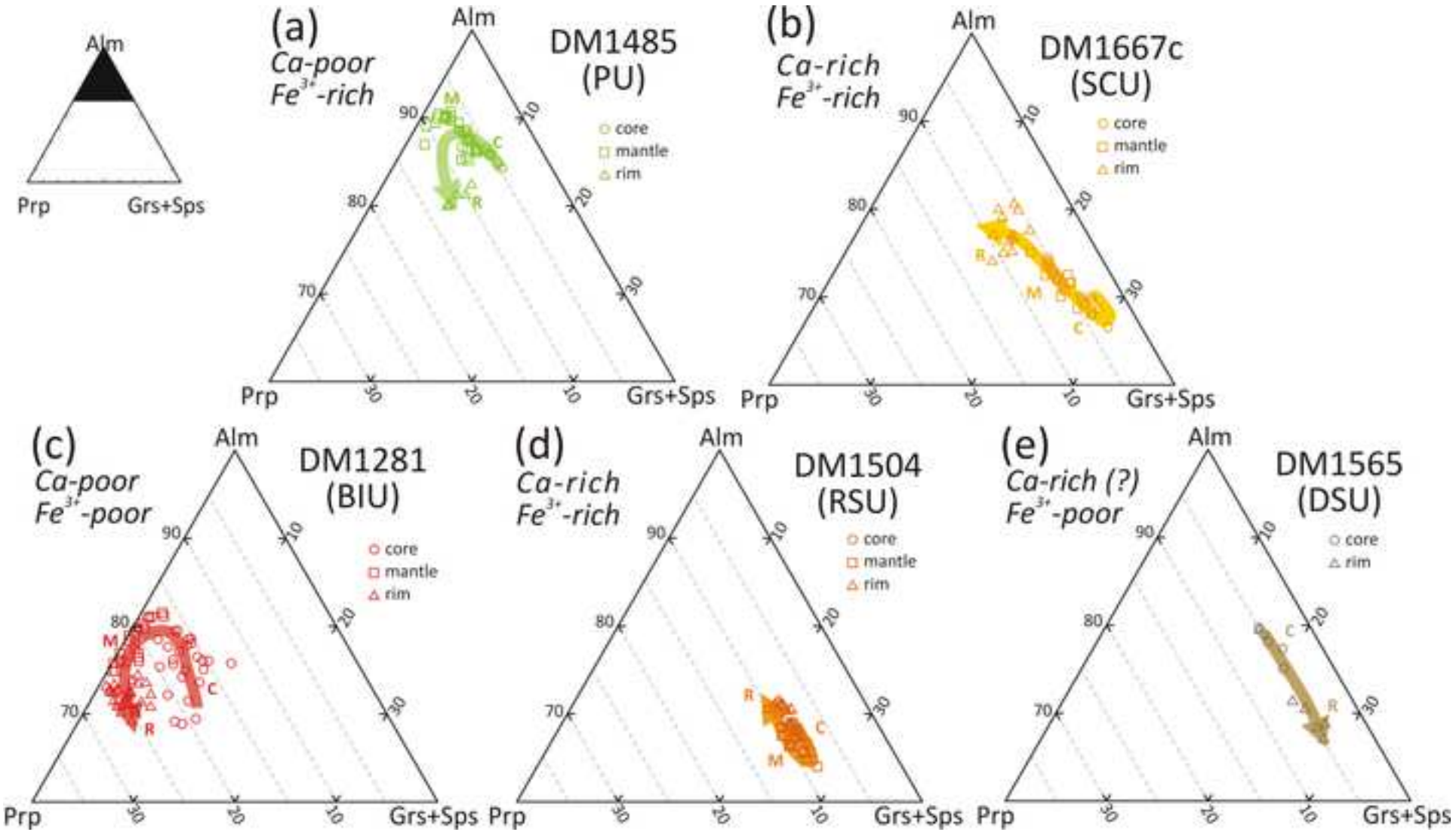

Fig. 7

Click here to access/download;Figure;Fig7.tif

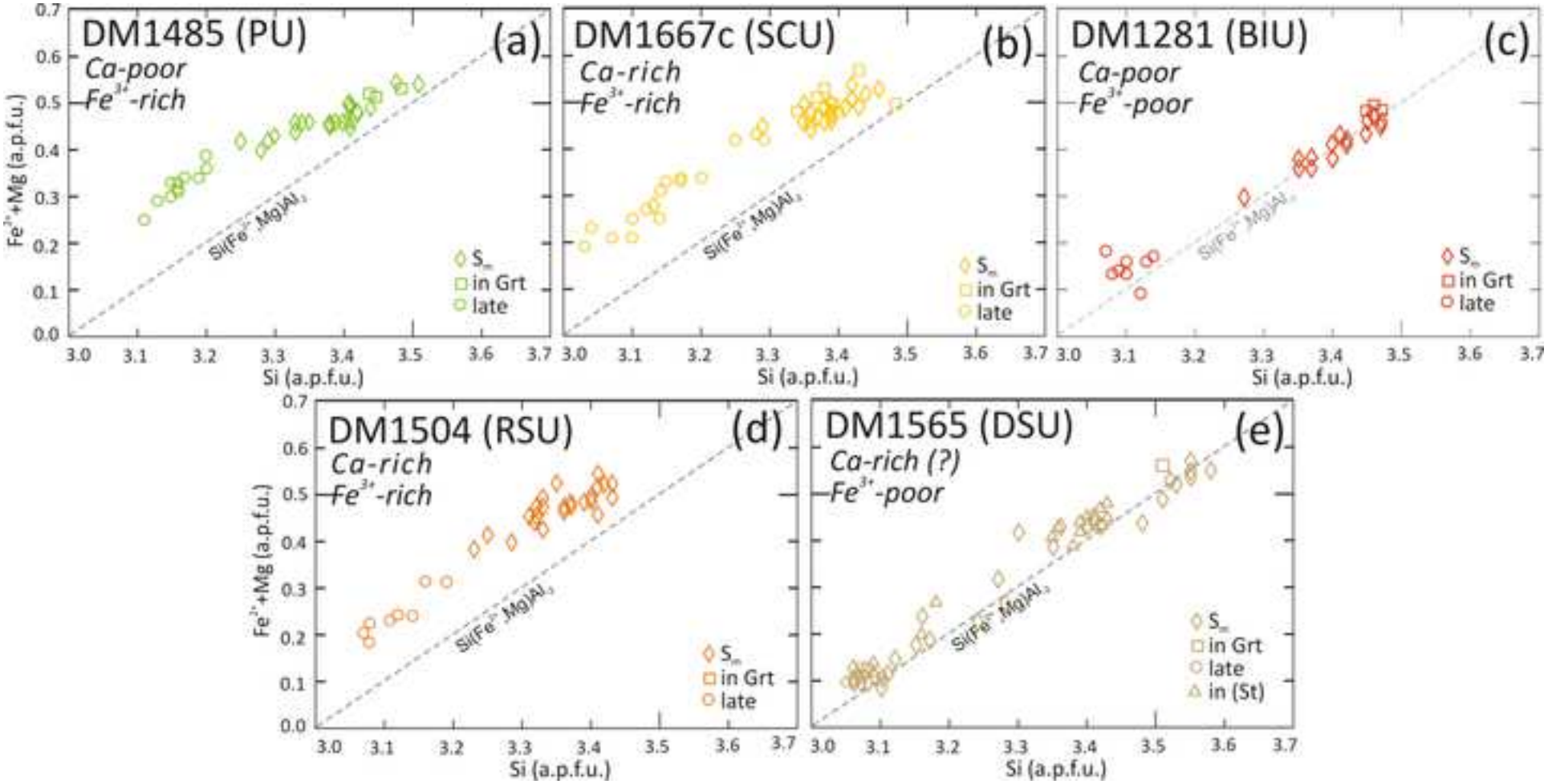

Fig. 8

Click here to access/download;Figure;Fig8.tif

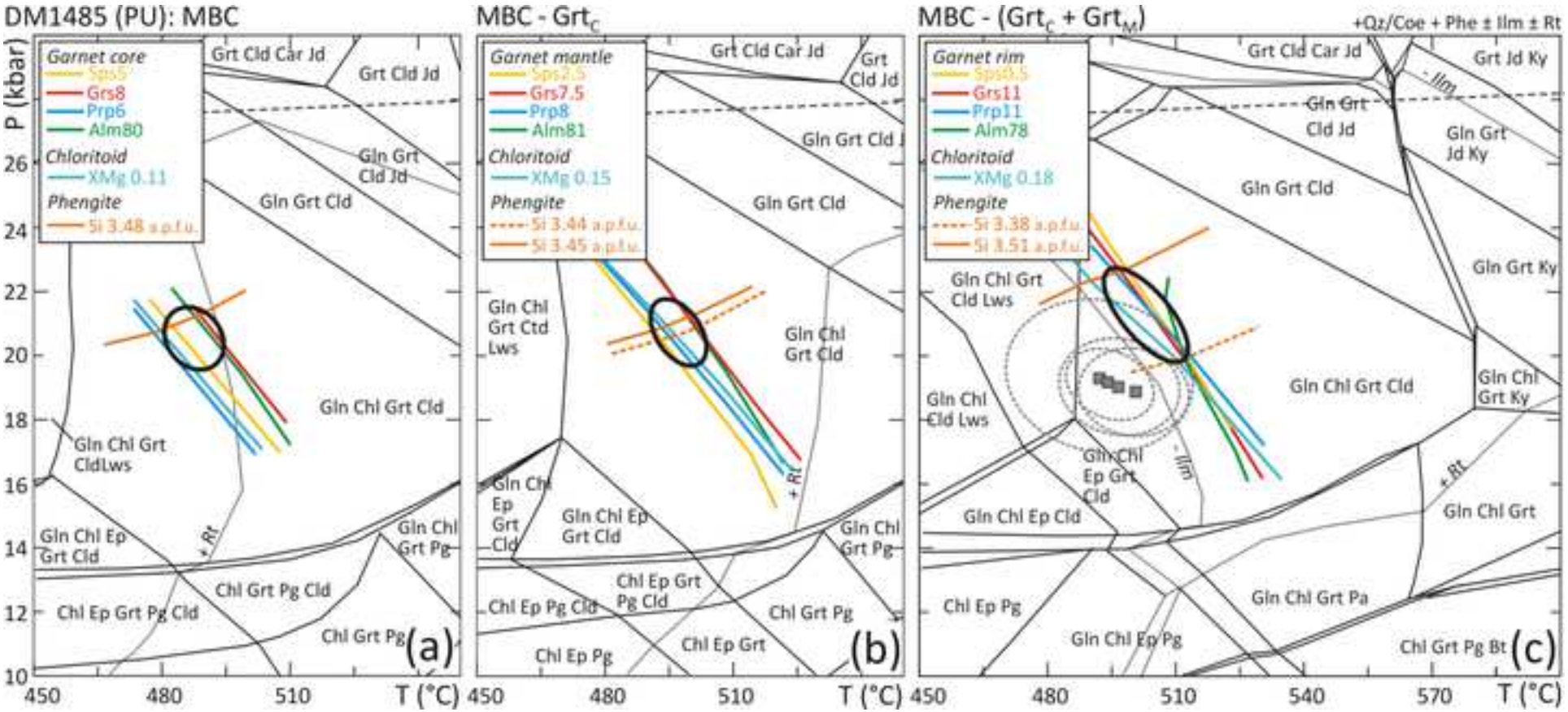

Fig. 9

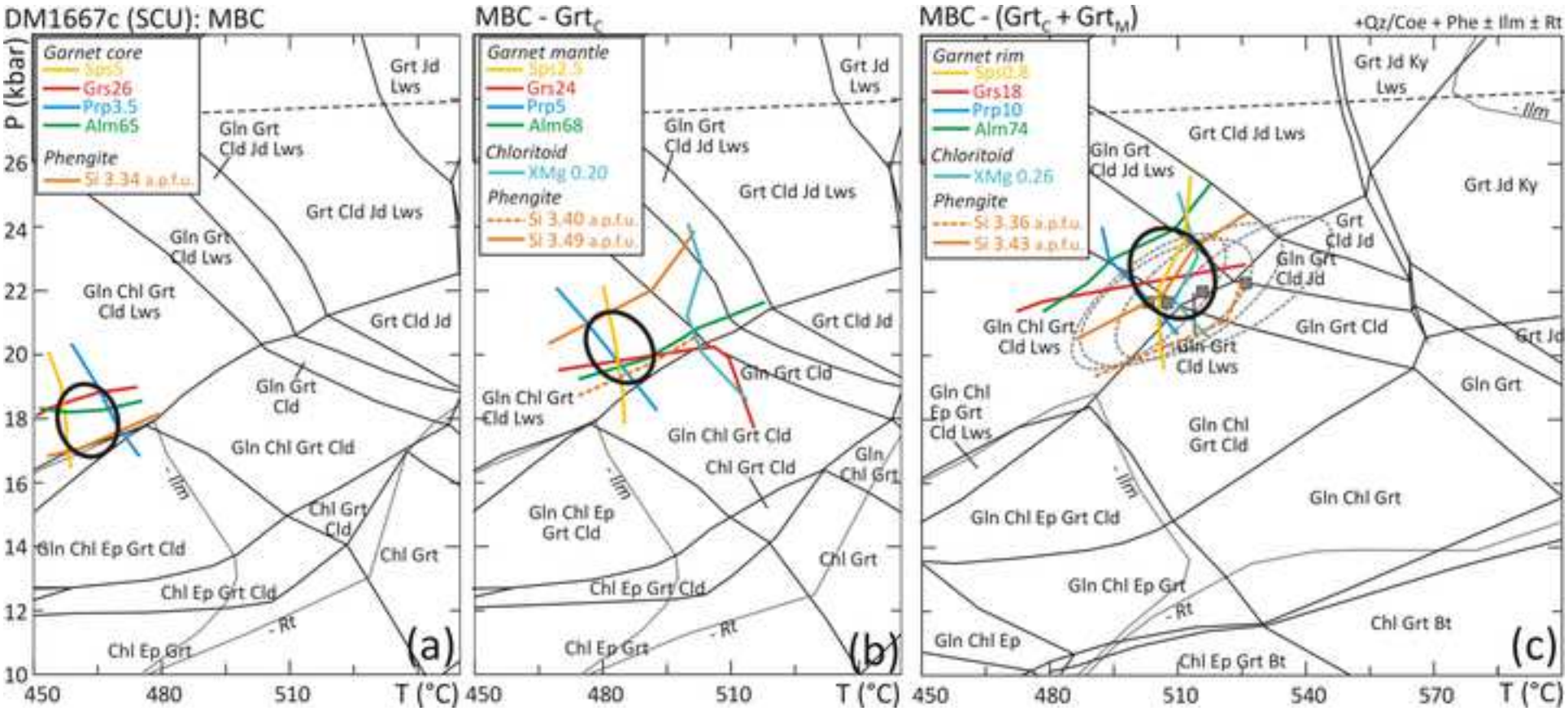

Fig. 10

Click here to access/download;Figure;Fig10.tif

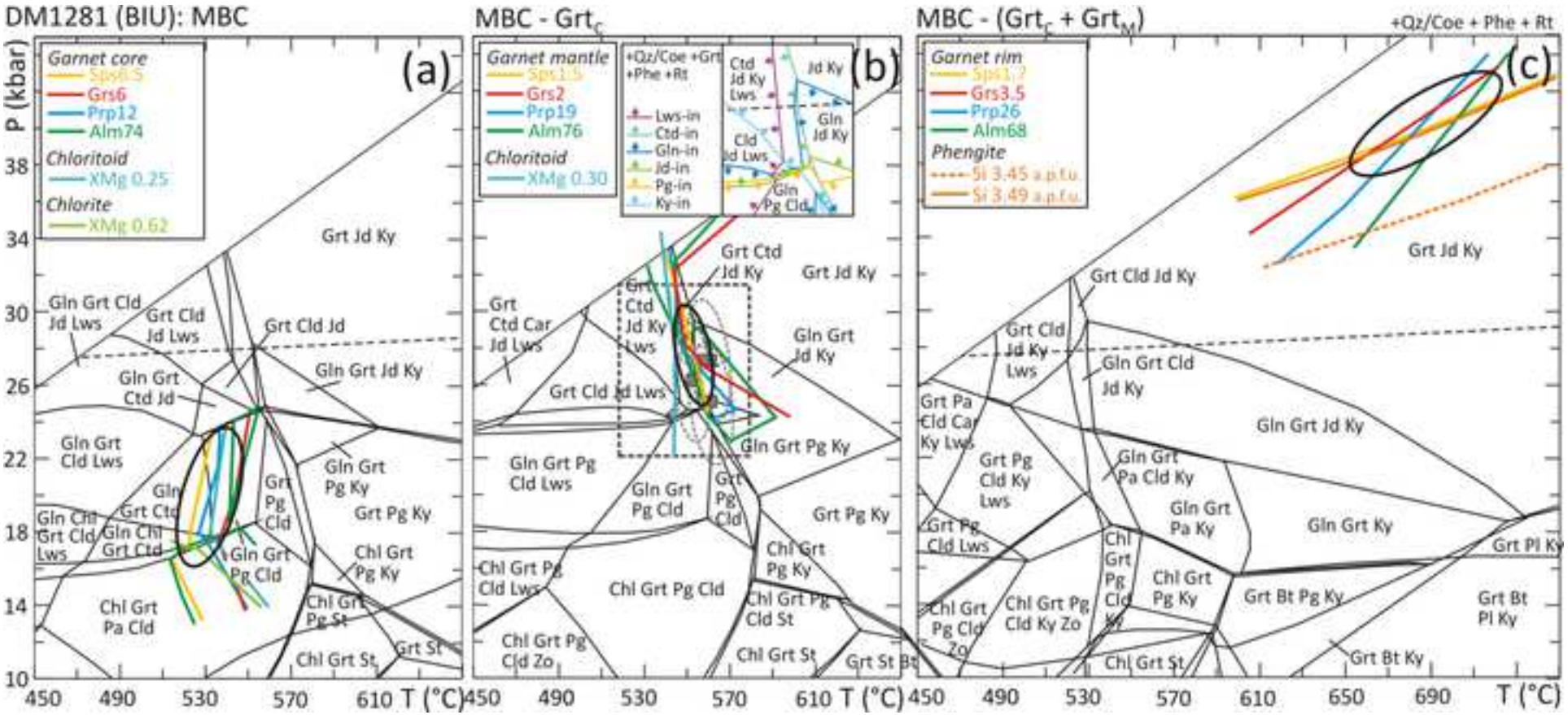

Fig. 11

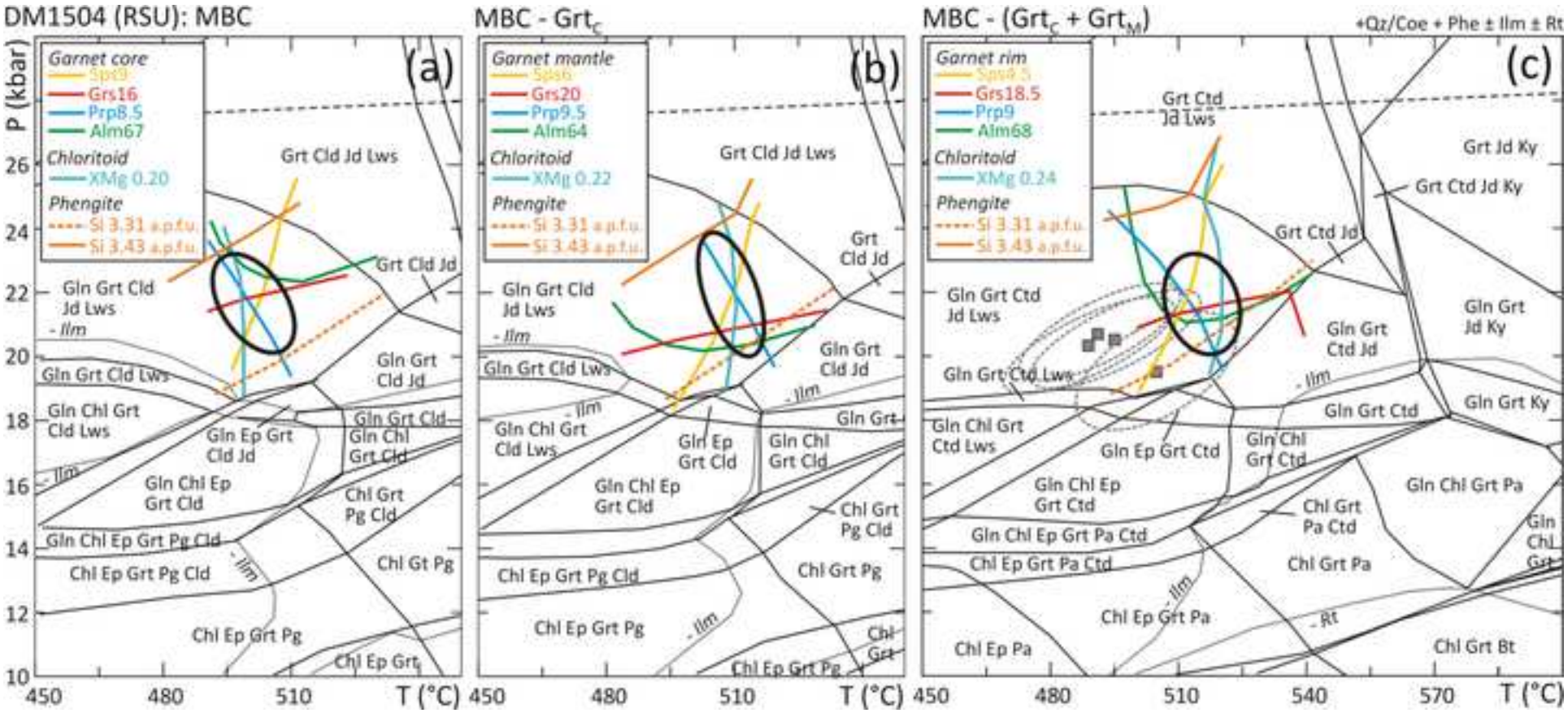

Fig. 12

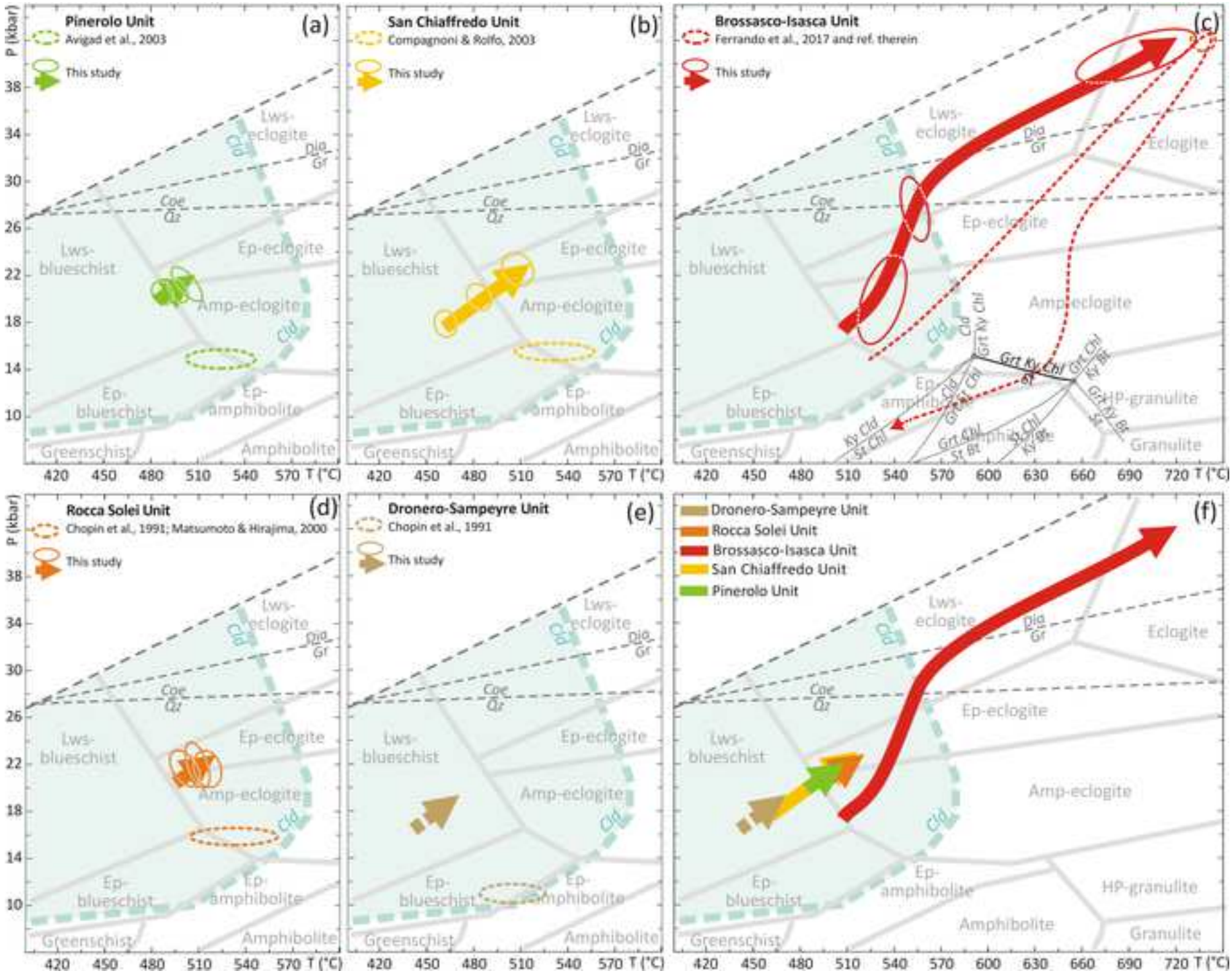

Table 1. Effective bulk-compositions (mol%) of the studied metapelites

Sample	DM1485 (PU)			DM1667c (SCU)			DM1281 (BIU)			DM1504 (RSU)		
	MBC	MBC-Grt_C	MBC-(Grt_C+Grt_R)	MBC	MBC-Grt_C	MBC-(Grt_C+Grt_R)	MBC	MBC-Grt_C	MBC-(Grt_C+Grt_R)	MBC	MBC-Grt_C	MBC-(Grt_C+Grt_R)
SiO_2	55.61	57.29	59.45	58.38	58.81	64.62	64.40	67.37	71.83	62.46	62.40	63.89
TiO_2	0.21	0.24	0.27	0.23	0.24	0.32	0.59	0.67	0.79	0.70	0.71	0.76
Al_2O_3	14.99	15.11	15.27	14.20	14.16	14.10	16.57	16.89	17.36	17.24	17.19	17.41
Fe_2O_3	1.07	0.92	0.73	0.94	0.92	0.61	0.00	0.00	0.00	0.53	0.51	0.43
FeO	16.67	14.50	11.42	14.74	14.45	9.60	9.84	6.71	2.01	7.84	8.07	6.78
MnO	0.38	0.12	0.02	0.33	0.27	0.06	0.29	0.09	0.02	0.28	0.23	0.05
MgO	6.99	7.54	8.12	4.03	4.09	4.80	4.23	3.93	3.00	4.20	4.19	4.21
CaO	0.76	0.56	0.46	4.27	4.09	1.84	0.49	0.26	0.15	1.68	1.60	0.98
Na_2O	0.68	0.77	0.88	0.32	0.33	0.45	0.75	0.85	1.00	0.90	0.91	0.98
K_2O	2.64	2.96	3.38	2.57	2.64	3.59	2.84	3.23	3.82	4.15	4.19	4.50

MBC = measured bulk-composition; MBC-Grt_C = effective bulk-composition after fractionation of Grt_C; MBC-(Grt_C+Grt_M) = effective bulk-composition after fractionation of Grt_C and Grt_M.

Table 2

Table 2. Average P-T estimates for the peak (DM1485, DM1667c, DM1504, DM1565) and late prograde (DM1281) assemblages of the studied samples

Sample	Assemblage (+Qz/Coe* + H_2O)	Phe Si a.p.f.u.	Grt XMg	Ctd XMg	Chl XMg	average T (°C)	error (σ) T (°C)	average P (kbar)	error (σ) P (kbar)	σfit	N° of reactions
DM1485 (PU)	Phe(6.1)-Grt(1.22)-Ctd(1.49)-Chl(4.7)	3.51	0.12	0.17	0.40	496	15	19	1.5	1.32	4
	Phe(2.31)-Grt(1.2)-Ctd(1.48)-Chl(4.8)	3.48	0.10	0.16	0.40	494	11	19.1	1.1	0.81	4
	Phe(6.11)-Grt(1.21)-Ctd(2.29)-Chl(4.9)	3.44	0.12	0.16	0.40	500	14	18.8	1.4	1.30	5
	Phe(6.6)-Grt(1.23)-Ctd(1.33)-Chl(3.7)	3.42	0.15	0.16	0.44	492	24	19.3	2.5	2.27	5
	*weighted mean***					*496*	*7*	*19.0*	*0.7*		
DM1667c (SCU)	Phe(7.17)-Grt(2.24)-Ctd(1.5)-Lws	3.46	0.08	0.28		526	16	22.3	1.7	0.78	4
	Phe(10.1)-Grt(9.22)-Ctd(2.52)-Lws	3.44	0.09	0.23		503	15	21.7	1.7	0.27	4
	Phe(10.9)-Grt(2.25)-Ctd(2.49)-Lws	3.44	0.10	0.23		515	16	22.0	1.8	0.76	3
	Phe(1.18)-Grt(9.1)-Ctd(2.40)-Lws	3.43	0.08	0.22		507	16	21.7	1.7	0.25	3
	*weighted mean***					*512*	*8*	*21.9*	*0.9*		
DM1281 (BIU)	Phe(12.2)-Grt(6.3)-Ctd(5.7)-Ky	3.47	0.24	0.31		560	9	27.5	2.9	1.03	3
	Phe(12.1)-Grt(6b.1)-Ctd(6.49)-Ky	3.45	0.25	0.30		552	9	26.3	2.7	0.43	3
	Phe(6.88)-Grt(6.32)-Ctd(6.36)-Ky	3.45	0.24	0.31		561	10	25.2	3.1	1.09	3
	Phe(8.3)-Grt(10.13)-Ctd(6.33)-Ky	3.46	0.24	0.29		557	9	27.5	0.4	0.83	4
	*weighted mean***					*557*	*5*	*27.4*	*0.4*		
DM1504 (RSU)	Phe(2.34)-Grt(2.2)-Ctd(2.35)-Gln(2.52)-Jd(2.44)-Lws	3.42	0.09	0.22		491	15	20.7	1.2	1.24	7
	Phe(6.21)-Grt(2.26)-Ctd(4.4)-Gln(2.52)-Jd(2.44)-Lws	3.43	0.10	0.23		505	16	19.5	1.6	1.22	5
	Phe(6.16)-Grt(1.19)-Ctd(6.8)-Gln(2.52)-Jd(2.44)-Lws	3.41	0.09	0.23		489	16	20.3	1.2	1.30	6
	Phe(6.3)-Grt(2.1)-Ctd(2.32)-Gln(2.52)-Jd(2.44)-Lws	3.43	0.09	0.23		495	16	20.5	1.2	1.31	7
	*weighted mean***					*495*	*8*	*20.3*	*0.6*		
DM1565 (DSU)	Phe(5.12)-Grt(3.15)-Ctd(2.3)-Lws	3.55	0.06	0.17		466	14	18.8	1.5	0.15	3
	Phe(5.6)-Grt(3.11)-Ctd(2.32)-Lws	3.55	0.05	0.18		446	14	16.4	1.3	0.29	3
	Phe(3.6)-Grt(7.1)-Ctd(2.25)-Lws	3.58	0.05	0.15		444	14	16.8	1.3	0.55	3
	*weighted mean***					*452*	*8*	*17.2*	*0.8*		

*Coe for sample DM1281

**Weighted mean (with error) implies that values with smaller errors weight more than values with bigger errors.

What's in the sandwich? New P-T constraints for the (U)HP nappe stack of southern Dora-Maira Massif (Western Alps)

submitted to ***European Journal of Mineralogy*** **(Ref: ejm190006)** by

Chiara Groppo, Simona Ferrando, Manuele Gilio, Serena Botta, Francesco Nosenzo, Gianni Balestro, Andrea Festa, Franco Rolfo

SUPPLEMENTARY MATERIAL

Sample locations

The five metapelite samples studied in this paper are part of the rich collection of thin sections from the southern DMM hosted at the Department of Earth Sciences of the University of Torino (Italy). Sample locations are reported in Fig. 1 and additional details are given below.

- **Sample DM1485 (PU)** was collected from a small (few metres) outcrop of garnet-bearing micaschists exposed at Case dei Canaveis, in the Comba Albetta valley (right tributary of the Po river, west of Sanfront).
- **Sample DM1667c (SCU)** was collected at Piano Pramalano, at the head of Isasca Valley (few tens of metres below the ridge separating the Isasca Valley from the Po Valley). Outcrop exposure is very poor and the sample was collected from the debris along the road; however, because the debris is totally composed of similar micaschists, we suppose that this is the dominant lithology of the area.
- **Sample DM1281 (BIU)** was collected from an outcrop located east of Piano la Ruota, at the head of the Rio Lavesio Valley (a right tributary of the Po river, south-west of Martiniana Po; the same small valley where there is the well-known locality of Case Parigi). The outcrop consists of a ten of metres thick level of metapelites hosted within augen-gneiss. A sample from the same outcrop was described by Compagnoni *et al*. (1994) in the guidebook for the field excursion organized for the 16th meeting of IMA.
- **Sample DM1504 (RSU)** was collected from a 20-50 m -thick layer of metapelites exposed on the ridge separating the Gilba Valley from the Po Valley, west of M. Scolagarda.
- **Sample DM1565 (DSU)** was collected close to the Santuario di Valmala at the head of the Valmala Valley, few hundred metres below the ridge between the Varaita and Maira Valleys. Henry (1990) described similar micaschists exposed south of Meira Palancia as “micaschistes amigdalaire” and reported the occurrence of relics of pre-Alpine staurolite only partially replaced by a fine-grained aggregate of chloritoid.

Compagnoni, R., Messiga, B., Castelli, D. (1994): High pressure metamorphism in the Western Alps. *in*: “Guidebook to the field excursion B1”, 16th General Meeting of the International Mineralogical Association, Pisa, Italy, 148 pp.

Henry, C. (1990): L’unité à coesite du massif Dora-Maira dans son cadre pétrologique et structurale (Alpes Occidentales, Italie). Thése Doctorat., Université Paris 6, 149 pp.

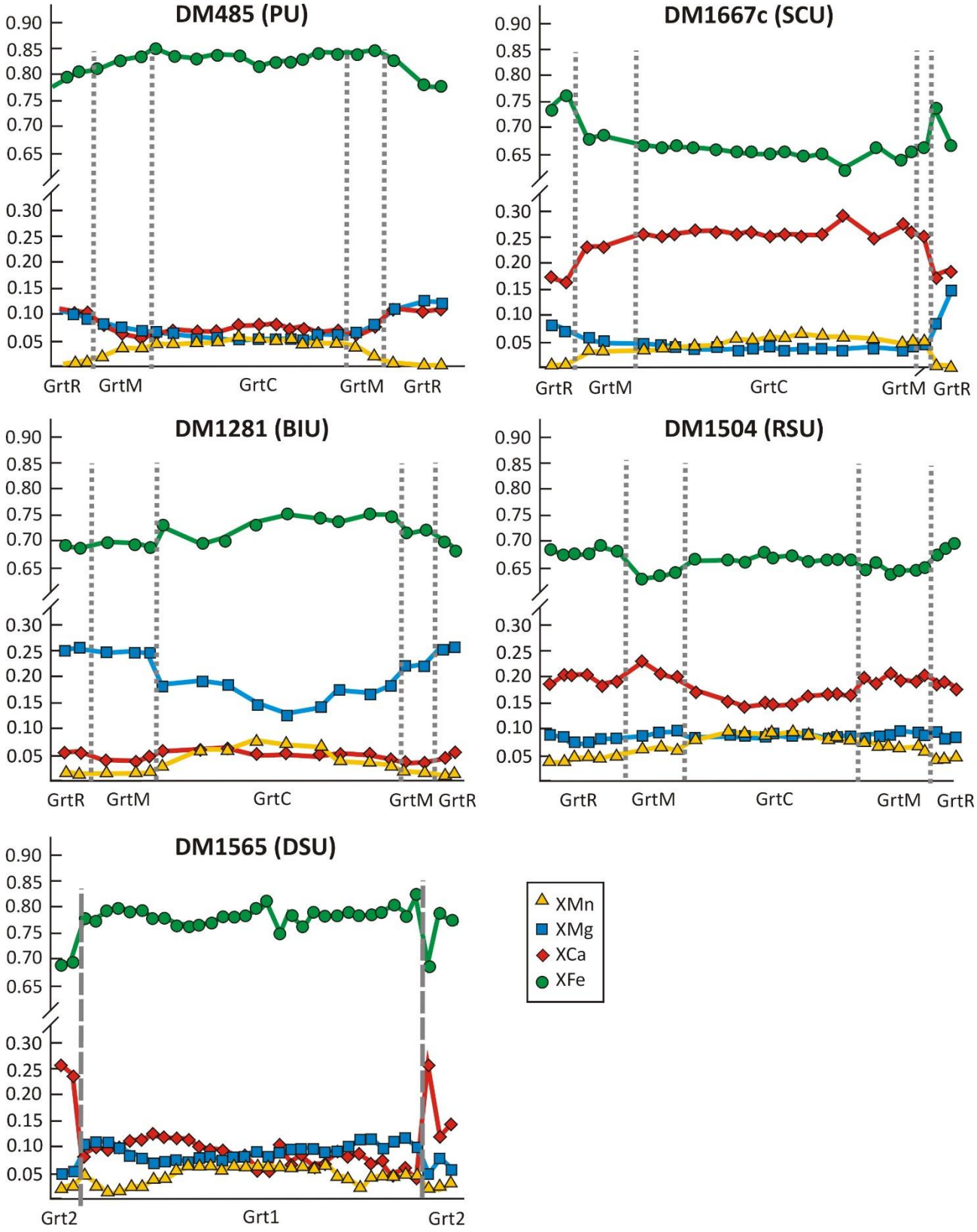

Fig. SM1 – Compositional profiles of garnet porphyroblasts from the investigated samples.

Table SM1a - Compositional variations of the main minerals in samples DM1485 (PU), DM1667c (SCU) and DM1281 (BIU)

DM1485 (PU)

Garnet	Sps	Prp	Grs	Alm
GrtC	4-6	5-7	7-9	80-83
GrtM	2-3	7-9	7-8	81-84
GrtR	0.3-1	9-12	10-11	77-81

Phengite	Si (a.p.f.u.)
Sm	3.38-3.51
in GrtC	3.48
in GrtM	3.44-3.45

Chloritoid	XMg
in GrtC	0.10-0.12
in GrtM	0.13-0.16
in GrtR	0.17-0.18

Chlorite	XMg
Sm	0.40-0.44
late	0.37-0.38

Biotite	XMg
late	0.38-0.40

DM1667c (SCU)

Garnet	Sps	Prp	Grs	Alm
GrtC	4-7	3-4	25-27	64-66
GrtM	2-3	4-6	18-19	73-75
GrtR	0.5-1	7-10	16-20	72-76
GrtO-R	1-2	5-7	18-19	73-75

Phengite	Si (a.p.f.u.)
Sm	3.35-3.46
in GrtC	3.34
in GrtM	3.40-3.49
in GrtR	3.36-3.43

Chloritoid	XMg
in GrtC/M	0.20-0.28
in GrtR	0.25-0.28

Chlorite	XMg
in GrtC/M	0.20-0.26
late	0.37-0.42

Epidote	XPs
in GrtC/M	0.50-0.84
late	0.32-0.46

Biotite	XMg
late	0.35-0.42

DM1281 (BIU)

Garnet	Sps	Prp	Grs	Alm
GrtC	3-8	12-16	5-6	73-77
GrtM	0.5-2	17-21	1-3	74-79
GrtR	1-2	22-26	3-5	68-72

Phengite	Si (a.p.f.u.)
Sm	3.35-3.49
in GrtR	3.45-3.47

Chloritoid	XMg
in GrtC/M	0.25-0.31

Chlorite	XMg
in GrtM	0.59-0.66
in GrtC	0.33-0.50

Staurolite	XMg
in GrtC/M	0.15-0.25

Table SM1b - Compositional variations of the main minerals in samples DM1504 (RSU) and DM1565 (DSU)

DM1504 (RSU)

Garnet	Sps	Prp	Grs	Alm
GrtC	7-10	8-9	14-18	66-69
GrtM	5-7	9-10	19-21	63-65
GrtR	4-5	8-10	17-20	66-70

Phengite	Si (a.p.f.u.)
Sm	3.31-3.43

Chloritoid	XMg
Sm CtdC	0.19-0.21
Sm CtdR	0.22-0.24
in GrtC	0.19-0.21
in GrtM	0.21-0.23
in GrtR	0.22-0.24

Glaucophane	XMg	XNa
in GrtM/R	0.38-0.42	0.91-0.94

Jadeite	XJd	XAeg
in GrtM/R	0.66-0.74	0.26-0.34

Epidote	XPs
late (in Grt)	0.53-0.63
late (matrix)	0.55-0.71

Chlorite	XMg
late	0.42-0.47

DM1565 (DSU)

Garnet 1	Sps	Prp	Grs	Alm
GrtC	3-7	6-9	5-10	75-80
GrtM	1-2	9.11	9-12	78-80
GrtR	2-5	10-12	4-9	78-82

Garnet 2	Sps	Prp	Grs	Alm
GrtC	2-4	4-5	14-16	75-78
GrtR	2-3	5-6	21-26	67-72

Phengite	Si (a.p.f.u.)
Sm	3.48-3.58

Chloritoid	XMg
Sm; after St	0.13-0.18

Chlorite	XMg
late	0.40-0.44

Table SM2a - Representative analyses of the main minerals in sample DM1485 (PU)

	White mica								Garnet					
Analysis	1.39 Phe	1.35 Phe	6.1 Phe*	2.31 Phe*	6.11 Phe*	6.6 Phe*	4.6 Ms	1.43 Pg	1.12 Grt	1.19 Grt	1.22 Grt*	1.2 Grt*	1.21 Grt*	1.23 Grt*
Site	In Grt_C	In Grt_M	// S_m	// S_m	// S_m	// S_m	late	In Grt_M	Core	Mantle	Rim	Rim	Rim	Rim
SiO_2	52.86	52.32	53.71	53.42	52.51	52.01	47.63	47.30	36.55	36.41	36.79	36.77	37.04	37.53
TiO_2	0.00	0.00	0.00	0.00	0.00	0.00	0.00	0.00	0.00	0.00	0.00	0.00	0.00	0.00
Al_2O_3	26.37	27.19	26.21	26.76	27.49	27.84	32.96	39.85	20.36	20.27	20.77	20.65	20.96	21.01
FeO	4.65	4.75	2.96	2.86	3.26	2.55	3.88	0.96	36.66	36.95	35.00	35.54	35.21	31.73
MnO	0.00	0.00	0.00	0.00	0.00	0.00	0.00	0.00	2.17	0.99	0.07	0.36	0.08	0.11
MgO	2.74	2.69	3.93	3.88	3.20	3.50	1.16	0.00	1.18	1.85	2.91	2.42	3.03	3.69
CaO	0.00	0.00	0.00	0.00	0.00	0.00	0.00	0.00	2.68	2.49	3.71	3.48	3.47	5.78
Na_2O	0.66	0.70	0.00	0.00	0.61	0.85	1.32	8.07	0.00	0.00	0.00	0.00	0.00	0.00
K_2O	9.15	9.18	9.90	9.98	9.54	9.39	9.16	0.00	0.00	0.00	0.00	0.00	0.00	0.00
Total	96.43	96.83	96.72	96.89	96.61	96.15	96.11	96.21	99.67	99.06	99.36	99.29	99.88	99.95
Si	3.48	3.44	3.51	3.48	3.44	3.42	3.16	2.99	2.99	2.99	2.98	2.99	2.98	2.98
Ti	0.00	0.00	0.00	0.00	0.00	0.00	0.00	0.00	0.00	0.00	0.00	0.00	0.00	0.00
Al	2.05	2.11	2.02	2.06	2.12	2.16	2.58	2.97	1.97	1.96	1.98	1.98	1.99	1.97
Fe^{+3}	0.00	0.00	0.00	0.00	0.00	0.00	0.00	0.02	0.04	0.06	0.07	0.05	0.06	0.06
Fe^{+2}	0.26	0.26	0.16	0.16	0.18	0.14	0.22	0.03	2.47	2.47	2.30	2.37	2.31	2.05
Mn	0.00	0.00	0.00	0.00	0.00	0.00	0.00	0.00	0.15	0.07	0.00	0.02	0.01	0.01
Mg	0.27	0.26	0.38	0.38	0.31	0.34	0.11	0.00	0.14	0.23	0.35	0.29	0.36	0.44
Ca	0.00	0.00	0.00	0.00	0.00	0.00	0.00	0.00	0.23	0.22	0.32	0.30	0.30	0.49
Na	0.08	0.09	0.00	0.00	0.08	0.11	0.17	0.99	0.00	0.00	0.00	0.00	0.00	0.00
K	0.00	0.00	0.83	0.83	0.80	0.79	0.78	0.00	0.00	0.00	0.00	0.00	0.00	0.00
XMg	0.51	0.50	0.70	0.71	0.64	0.71	0.35	0.00	0.05	0.08	0.12	0.10	0.12	0.15
XFe									0.82	0.83	0.77	0.79	0.78	0.69
XCa									0.08	0.07	0.11	0.10	0.10	0.17
XMn									0.05	0.02	0.00	0.01	0.00	0.00

* Analysis used for AvPT calculations (see Table 2)

Structural formulae have been calculated on the basis of 11 oxygens for white mica and 12 oxygens for garnet.

Fe^{3+} has been calculated by stoichiometry

Table SM2b - Representative analyses of the main minerals in sample DM1485 (PU)

	Chloritoid						Chlorite			
Analysis	1.28 Cld	1.46 Cld	1.49 Cld*	1.48 Cld*	2.29 Cld*	1.33 Cld*	4.7 Chl*	4.8 Chl*	4.9 Chl*	3.7 Chl*
Site	In Grt_C	In Grt_M	In Grt_R	In Grt_R	In Grt_R	In Grt_R	// S_m	// S_m	// S_m	// S_m
SiO_2	24.60	24.60	24.59	25.10	24.63	24.91	24.60	25.05	24.62	25.45
TiO_2	0.00	0.00	0.00	0.00	0.00	0.00	0.00	0.00	0.00	0.00
Al_2O_3	39.72	39.51	39.61	40.40	40.21	40.08	22.03	21.78	21.81	21.82
FeO	27.10	26.47	25.87	25.42	25.40	25.82	30.44	30.65	30.38	28.90
MnO	0.00	0.00	0.00	0.00	0.00	0.00	0.00	0.00	0.00	0.00
MgO	1.77	2.38	2.91	2.80	2.79	2.72	11.27	11.39	11.47	12.50
CaO	0.00	0.00	0.00	0.00	0.00	0.00	0.00	0.00	0.00	0.00
Na_2O	0.00	0.00	0.00	0.00	0.00	0.00	0.00	0.00	0.00	0.00
K_2O	0.00	0.00	0.00	0.00	0.00	0.00	0.00	0.00	0.00	0.00
Total	93.28	93.1	93.17	93.77	93.13	93.63	88.34	88.87	88.28	88.68
Si	2.04	2.03	2.02	2.05	2.02	2.04	2.65	2.68	2.65	2.71
Ti	0.00	0.00	0.00	0.00	0.00	0.00	0.00	0.00	0.00	0.00
Al	3.87	3.85	3.84	3.88	3.89	3.86	2.80	2.75	2.77	2.74
Fe^{+3}	0.06	0.09	0.11	0.03	0.06	0.06	0.00	0.00	0.00	0.00
Fe^{+2}	1.82	1.74	1.67	1.71	1.68	1.71	2.74	2.75	2.74	2.57
Mn	0.00	0.00	0.00	0.00	0.00	0.00	0.00	0.00	0.00	0.00
Mg	0.22	0.29	0.36	0.34	0.34	0.33	1.81	1.82	1.84	1.98
Ca	0.00	0.00	0.00	0.00	0.00	0.00	0.00	0.00	0.00	0.00
Na	0.00	0.00	0.00	0.00	0.00	0.00	0.00	0.00	0.00	0.00
K	0.00	0.00	0.00	0.00	0.00	0.00	0.00	0.00	0.00	0.00
XMg	0.11	0.14	0.18	0.17	0.17	0.16	0.40	0.40	0.40	0.44

* Analysis used for AvPT calculations (see Table 2)

Structural formulae have been calculated on the basis of 14 oxygens for chloritoid and 18 oxygens for chlorite.

Fe^{3+} has been calculated by stoichiometry

Table SM3a - Representative analyses of the main minerals in sample DM1667c (SCU)

	White mica								Garnet					
Analysis	9.28 Phe	9.29 Phe	7.19 Phe	7.17 Phe*	10.1 Phe*	10.9 Phe*	1.18 Phe*	2.27 Pa	9.11 Grt	9.4 Grt	2.24 Grt*	9.22 Grt*	2.25 Grt*	9.1 Grt*
Site	In Grt_C	In Grt_M	In Grt_R	// S_m	// S_m	// S_m	// S_m	In Grt_M	Core	Mantle	Rim	Rim	Rim	Rim
SiO_2	50.42	53.00	51.56	52.25	52.44	52.22	52.28	47.14	36.70	36.79	37.01	36.82	36.55	37.04
TiO_2	0.45	0.00	0.38	0.00	0.00	0.00	0.00	0.00	0.00	0.00	0.00	0.00	0.00	0.00
Al_2O_3	28.68	26.56	26.26	26.59	27.00	27.25	27.66	40.04	20.15	20.50	20.73	20.69	20.24	20.57
FeO	3.36	3.52	4.36	3.55	3.41	3.88	3.35	0.63	30.67	31.54	33.16	33.87	32.36	33.46
MnO	0.00	0.00	0.00	0.00	0.00	0.00	0.00	0.00	2.35	1.48	0.49	0.32	0.82	0.34
MgO	2.90	3.15	3.36	3.32	3.40	3.18	3.19	0.00	0.88	1.23	1.95	2.12	2.36	2.07
CaO	0.00	0.00	0.00	0.00	0.00	0.00	0.00	0.32	8.81	7.97	6.18	5.80	6.52	5.97
Na_2O	0.91	0.87	0.56	0.62	0.57	0.00	0.58	7.72	0.00	0.00	0.00	0.00	0.00	0.00
K_2O	9.47	9.00	9.76	9.78	9.98	10.18	9.86	0.21	0.00	0.00	0.00	0.00	0.00	0.00
Total	96.19	96.10	96.24	96.11	96.80	96.71	96.92	96.06	99.55	99.52	99.53	99.62	98.85	99.46
Si	3.34	3.49	3.43	3.46	3.44	3.44	3.43	2.99	2.970	2.974	2.987	2.970	2.964	2.992
Ti	0.02	0.00	0.02	0.00	0.00	0.00	0.00	0.00	0.00	0.00	0.00	0.00	0.00	0.00
Al	2.24	2.06	2.06	2.07	2.09	2.11	2.14	2.99	1.923	1.953	1.972	1.967	1.934	1.959
Fe^{+3}	0.00	0.00	0.00	0.00	0.00	0.00	0.00	0.00	0.137	0.099	0.054	0.094	0.139	0.057
Fe^{+2}	0.19	0.19	0.24	0.20	0.19	0.21	0.18	0.03	1.940	2.034	2.184	2.192	2.056	2.203
Mn	0.00	0.00	0.00	0.00	0.00	0.00	0.00	0.00	0.161	0.102	0.034	0.022	0.056	0.023
Mg	0.29	0.31	0.33	0.33	0.33	0.31	0.31	0.00	0.106	0.149	0.235	0.255	0.285	0.249
Ca	0.00	0.00	0.00	0.00	0.00	0.00	0.00	0.02	0.764	0.690	0.535	0.501	0.567	0.517
Na	0.12	0.11	0.07	0.08	0.07	0.00	0.07	0.95	0.00	0.00	0.00	0.00	0.00	0.00
K	0.80	0.76	0.83	0.83	0.84	0.85	0.82	0.02	0.00	0.00	0.00	0.00	0.00	0.00
XMg	0.606	0.615	0.579	0.625	0.64	0.594	0.629	0.00	0.04	0.05	0.08	0.09	0.10	0.08
XFe									0.65	0.68	0.73	0.74	0.69	0.74
XCa									0.26	0.23	0.18	0.17	0.19	0.17
XMn									0.05	0.03	0.01	0.01	0.02	0.01

* Analysis used for AvPT calculations (see Table 2)

Structural formulae have been calculated on the basis of 11 oxygens for white mica and 12 oxygens for garnet.

Fe^{3+} has been calculated by stoichiometry

Table SM3b - Representative analyses of the main minerals in sample DM1667c (SCU)

	Chloritoid				Epidote		Chlorite	
Analysis	1.5 Cld*	2.52 Cld*	2.49 Cld*	2.40 Cld*	11.12 Ep	9.27 Ep	1.22 Chl	3.1 Chl
Site	In Grt_R	In Grt_M	In Grt_M	In Grt_M	In Grt_C	In (Lws)	In Grt_C	late
SiO_2	25.13	25.35	25.13	25.01	38.47	38.63	23.59	24.66
TiO_2	0.00	0.00	0.00	0.00	0.00	0.00	0.00	0.00
Al_2O_3	40.92	40.67	40.86	40.67	25.47	29.15	20.32	21.54
FeO	22.61	23.72	23.15	23.55	10.63	6.15	37.03	31.18
MnO	4.82	4.03	3.92	3.74	0.00	0.00	0.55	0.00
MgO	0.00	0.00	0.00	0.00	0.00	0.00	7.01	11.43
CaO	0.00	0.00	0.00	0.00	22.15	23.56	0.00	0.00
Na_2O	0.00	0.00	0.00	0.00	0.00	0.00	0.00	0.00
K_2O	0.00	0.00	0.00	0.00	0.00	0.00	0.00	0.00
Total	93.48	93.77	93.05	92.97	96.72	97.49	88.50	88.82
Si	2.02	2.05	2.04	2.04	3.02	2.99	2.64	2.65
Ti	0.00	0.00	0.00	0.00	0.00	0.00	0.00	0.00
Al	3.88	3.87	3.91	3.91	2.36	2.65	2.68	2.72
Fe^{+3}	0.08	0.04	0.01	0.02	0.70	0.40	0.04	0.00
Fe^{+2}	1.44	1.56	1.57	1.58	0.00	0.00	3.42	2.80
Mn	0.00	0.00	0.00	0.00	0.00	0.00	0.05	0.00
Mg	0.58	0.49	0.47	0.45	0.00	0.00	1.17	1.83
Ca	0.00	0.00	0.00	0.00	1.86	1.95	0.00	0.00
Na	0.00	0.00	0.00	0.00	0.00	0.00	0.00	0.00
K	0.00	0.00	0.00	0.00	0.00	0.00	0.00	0.00
XMg	0.28	0.23	0.23	0.22			0.25	0.40
XPs					0.64	0.36		

* Analysis used for AvPT calculations (see Table 2)

Structural formulae have been calculated on the basis of 14 oxygens for chloritoid, 12 oxygens for epidote and 18 oxygens for chlorite.

Fe^{3+} has been calculated by stoichiometry

Table SM4a - Representative analyses of the main minerals in sample DM1281 (BIU)

	White mica							Garnet					
Analysis	12.2Phe*	12.1 Phe*	6.88 Phe*	8.3 Phe*	9.23 Phe	10.20 Ms	6.51 Pa	Grt 11.10	6.3 Grt*	6b.1 Grt*	6.32 Grt*	10.13Grt*	6.1 Grt
Site	// S_m	// S_m	// S_m	// S_m	In Grt_R	In Grt_C	In Grt_C	Core	Mantle	Mantle	Mantle	Mantle	Rim
SiO_2	53.17	52.77	52.96	53.02	53.11	47.77	47.39	37.07	37.28	37.86	37.43	37.71	37.85
TiO_2	0.40	0.47	0.00	0.00	0.00	0.00	0.00	0.00	0.00	0.00	0.00	0.00	0.00
Al_2O_3	27.15	27.20	28.20	27.27	27.23	36.21	40.38	21.08	21.33	21.40	21.22	21.37	21.67
FeO	1.65	1.72	1.48	1.77	1.81	1.48	0.00	33.55	33.98	31.76	33.77	33.72	32.23
MnO	0.00	0.00	0.00	0.00	0.00	0.00	0.00	3.21	0.08	0.64	0.23	0.20	0.53
MgO	3.77	3.82	3.64	3.81	3.92	0.81	0.60	3.09	5.93	6.23	6.12	6.07	6.57
CaO	0.00	0.00	0.00	0.00	0.00	0.00	0.00	1.79	0.43	1.63	0.31	0.59	0.98
Na_2O	0.00	0.00	0.00	0.51	0.66	2.11	7.35	0.00	0.00	0.00	0.00	0.00	0.00
K_2O	10.34	10.52	10.32	10.38	9.42	8.20	0.40	0.00	0.00	0.00	0.00	0.00	0.00
Total	96.48	96.50	96.60	96.75	96.16	96.58	96.13	99.79	99.03	99.52	99.07	99.66	99.82
Si	3.47	3.45	3.45	3.46	3.47	3.10	3.01	2.99	2.977	2.992	2.985	2.988	2.980
Ti	0.02	0.02	0.00	0.00	0.00	0.00		0.00	0.00	0.00	0.00	0.00	0.00
Al	2.09	2.10	2.16	2.10	2.10	2.77	3.02	2.00	2.007	1.993	1.995	1.9957	2.010
Fe^{+3}	0.00	0.00	0.00	0.00	0.00	0.00	0.00	0.02	0.040	0.022	0.036	0.0282	0.031
Fe^{+2}	0.09	0.09	0.08	0.10	0.10	0.08	0.03	2.24	2.229	2.078	2.216	2.2069	2.092
Mn	0.00	0.00	0.00	0.00	0.00	0.00	0.00	0.22	0.006	0.043	0.016	0.0137	0.035
Mg	0.37	0.37	0.35	0.37	0.38	0.08	0.00	0.37	0.706	0.733	0.727	0.7172	0.770
Ca	0.00	0.00	0.00	0.00	0.00	0.00	0.00	0.15	0.037	0.138	0.026	0.0503	0.083
Na	0.00	0.00	0.00	0.06	0.08	0.27	0.91	0.00	0.00	0.00	0.00	0.00	0.00
K	0.86	0.88	0.86	0.86	0.79	0.68	0.03	0.00	0.00	0.00	0.00	0.00	0.00
XMg	0.80	0.80	0.82	0.79	0.79	0.49	0.00	0.12	0.24	0.25	0.24	0.24	0.26
XFe								0.75	0.75	0.69	0.74	0.74	0.70
XCa								0.05	0.01	0.05	0.01	0.02	0.03
XMn								0.07	0.00	0.01	0.01	0.01	0.01

* Analysis used for AvPT calculations (see Table 2)

Structural formulae have been calculated on the basis of 11 oxygens for white mica and 12 oxygens for garnet.

Fe^{3+} has been calculated by stoichiometry

Table SM4b - Representative analyses of the main minerals in sample DM1281 (BIU)

	Chloritoid				Chlorite		Staurolite	
Analysis	5.7 Cld*	6.49 Cld*	6.36 Cld*	6.33 Cld*	6.52 Chl	10.24 Chl	6b.5 St	11.26 St
Site	In Grt_M	In Grt_M	In Grt_M	In Grt_M	In Grt_C	late	In Grt_C	In Grt_C
SiO_2	25.88	25.58	25.75	25.54	27.56	24.03	30.70	29.57
TiO_2	0.00	0.00	0.00	0.00	0.00	0.00	0.00	0.35
Al_2O_3	41.99	41.84	41.94	41.35	22.34	22.89	57.68	55.21
FeO	20.36	21.29	20.79	21.25	18.58	32.13	9.36	10.64
MnO	0.00	0.00	0.00	0.00	0.00	0.00	0.00	0.00
MgO	5.24	5.07	5.12	4.89	20.06	9.64	1.11	1.75
CaO	0.00	0.00	0.00	0.00	0.00	0.00	0.00	0.00
Na_2O	0.00	0.00	0.00	0.00	0.00	0.00	0.00	0.00
K_2O	0.00	0.00	0.00	0.00	0.00	0.00	0.00	0.00
Total	93.47	93.78	93.60	93.02	88.54	88.70	98.85	97.52
Si	2.07	2.04	2.06	2.06	2.77	2.61	4.26	4.17
Ti	0.00	0.00	0.00	0.00	0.00	0.00	0.00	0.04
Al	3.95	3.94	3.95	3.92	2.65	2.92	9.43	9.17
Fe^{+3}	0.00	0.00	0.00	0.00	0.00	0.00	0.00	0.00
Fe^{+2}	1.36	1.42	1.39	1.43	1.56	2.91	1.09	1.25
Mn	0.00	0.00	0.00	0.00	0.00	0.00	0.00	0.00
Mg	0.62	0.60	0.61	0.59	3.01	1.56	0.23	0.37
Ca	0.00	0.00	0.00	0.00	0.00	0.00	0.00	0.00
Na	0.00	0.00	0.00	0.00	0.00	0.00	0.00	0.00
K	0.00	0.00	0.00	0.00	0.00	0.00	0.00	0.00
XMg	0.31	0.30	0.31	0.29	0.66	0.35	0.18	0.23

* Analysis used for AvPT calculations (see Table 2)

Structural formulae have been calculated on the basis of 14 oxygens for chloritoid, 18 oxygens for chlorite and 12 oxygens for staurolite.

Fe^{3+} has been calculated by stoichiometry

Table SM5a - Representative analyses of the main minerals in sample DM1504 (RSU)

	White mica						Garnet					
Analysis	2.34 Phe*	6.21 Phe*	6.16 Phe*	6.3 Phe*	7.20 Ms	6.15 Pa	2.16 Grt	2.8 Grt	2.2 Grt*	2.26 Grt*	1.19 Grt*	2.1 Grt*
Site	In Grt_R	// S_m	// S_m	In Cld	late	⊥ Sm	Core	Mantle	Rim	Rim	Rim	Rim
SiO_2	51.86	52.08	51.42	52.38	47.24	48.40	37.09	37.09	37.47	36.88	37.19	37.21
TiO_2	0.00	0.00	0.00	0.00	0.00	0.00	0.00	0.00	0.00	0.00	0.00	0.00
Al_2O_3	27.60	27.64	27.34	27.47	35.02	39.39	20.78	20.52	20.39	20.48	20.87	20.40
FeO	3.79	3.66	4.31	3.85	2.85	0.65	30.05	29.49	30.70	31.04	29.44	31.13
MnO	0.00	0.00	0.00	0.00	0.00	0.00	3.99	2.91	1.66	1.83	2.79	1.72
MgO	3.01	3.01	3.05	3.19	0.67	0.00	2.09	2.30	2.14	2.37	2.35	2.21
CaO	0.00	0.00	0.00	0.00	0.00	0.00	5.63	7.15	7.13	6.39	7.19	6.54
Na_2O	0.58	0.00	0.78	0.72	1.92	7.68	0.00	0.00	0.00	0.00	0.00	0.00
K_2O	9.75	10.35	9.46	9.32	8.33	0.24	0.00	0.00	0.00	0.00	0.00	0.00
Total	96.59	96.74	96.36	96.93	96.02	96.37	99.63	99.46	99.50	98.99	99.83	99.22
Si	3.42	3.43	3.41	3.43	3.11	3.06	2.99	2.98	3.02	2.98	2.98	3.01
Ti	0.00	0.00	0.00	0.00	0.00	0.00	0.00	0.00	0.00	0.00	0.00	0.00
Al	2.14	2.14	2.13	2.12	2.72	2.94	1.97	1.94	1.93	1.95	1.97	1.94
Fe^{+3}	0.00	0.00	0.00	0.00	0.00	0.00	0.05	0.09	0.04	0.08	0.08	0.05
Fe^{+2}	0.21	0.20	0.24	0.21	0.16	0.03	1.98	1.89	2.03	2.02	1.89	2.05
Mn	0.00	0.00	0.00	0.00	0.00	0.00	0.27	0.20	0.11	0.13	0.19	0.12
Mg	0.30	0.29	0.30	0.31	0.07	0.00	0.25	0.28	0.26	0.29	0.28	0.27
Ca	0.00	0.00	0.00	0.00	0.00	0.00	0.49	0.62	0.62	0.55	0.62	0.57
Na	0.07	0.00	0.10	0.09	0.25	0.94	0.00	0.00	0.00	0.00	0.00	0.00
K	0.82	0.87	0.80	0.78	0.70	0.02						
XMg	0.59	0.59	0.56	0.60	0.295	0.00	0.08	0.09	0.09	0.10	0.09	0.09
XFe							0.66	0.64	0.67	0.68	0.64	0.68
XCa							0.16	0.21	0.20	0.19	0.21	0.19
XMn							0.09	0.07	0.04	0.04	0.06	0.04

* Analysis used for AvPT calculations (see Table 2)

Structural formulae have been calculated on the basis of 11 oxygens for white mica and 12 oxygens for garnet.

Fe^{3+} has been calculated by stoichiometry

Table SM5b - Representative analyses of the main minerals in sample DM1504 (RSU)

	Chloritoid							Jadeite	Glaucophane
Analysis	7.9 Cld	1.22 Cld	1.20 Cld	6.8 Cld*	2.35 Cld*	4.4 Cld*	2.32 Cld*	2.44 Jd*	2.52 Gln*
Site	Core	In Grt_C	In Grt_M	Rim	In Grt_R	In Grt_R	In Grt_R	In Grt_R	In Grt_R
SiO_2	25.22	25.22	25.11	25.18	25.14	24.77	24.58	56.79	55.54
TiO_2	0.00	0.00	0.00	0.00	0.00	0.00	0.00	0.00	0.00
Al_2O_3	40.44	40.63	40.61	40.21	40.66	40.29	39.98	17.49	9.58
FeO	24.17	23.91	23.74	23.86	23.60	23.61	23.43	8.69	18.07
MnO	0.54	0.00	0.46	0.00	0.00	0.42	0.42	0.00	0.00
MgO	3.25	3.61	3.80	4.07	3.69	3.84	3.81	0.00	7.34
CaO	0.00	0.00	0.00	0.00	0.00	0.00	0.00	0.47	0.76
Na_2O	0.00	0.00	0.00	0.00	0.00	0.00	0.00	14.62	6.53
K_2O	0.00	0.00	0.00	0.00	0.00	0.00	0.00	0.00	0.00
Total	93.62	93.38	93.72	93.32	93.09	92.93	92.22	98.06	97.83
Si	2.05	2.05	2.03	2.04	2.05	2.02	2.05	2.00	7.83
Ti	0.00	0.00	0.00	0.00	0.00	0.00	0.00	0.00	0.00
Al	3.87	3.89	3.87	3.85	3.90	3.87	3.87	0.73	1.59
Fe^{+3}	0.02	0.01	0.06	0.07	0.01	0.09	0.04	0.26	0.53
Fe^{+2}	1.62	1.61	1.54	1.55	1.60	1.52	1.56	0.00	1.60
Mn	0.04	0.00	0.03	0.00	0.00	0.03	0.03	0.00	0.00
Mg	0.39	0.44	0.46	0.49	0.45	0.47	0.46	0.00	1.54
Ca	0.00	0.00	0.00	0.00	0.00	0.00	0.00	0.02	0.11
Na	0.00	0.00	0.00	0.00	0.00	0.00	0.00	1.00	1.79
K	0.00	0.00	0.00	0.00	0.00	0.00	0.00	0.00	0.00
XMg	0.20	0.21	0.23	0.23	0.22	0.23	0.23	0.00	0.48
XNa								0.98	0.94

* Analysis used for AvPT calculations (see Table 2)

Structural formulae have been calculated on the basis of 14 oxygens for chloritoid, 6 oxygens for jadeite and 24 oxygens for glaucophane.

Fe^{3+} has been calculated by stoichiometry

Table SM6a - Representative analyses of the main minerals in sample DM1565 (DSU)

	White mica						Pre-Alpine Garnet (Grt_1)			Alpine Garnet (Grt_2)			
Analysis	5.12 Phe*	5.6 Phe*	3.6 Phe*	2.27 Phe	8.18 Ms	5.3 Pa	1.16 Grt	t 1.6 Grt	1.30 Grt	3.13 Grt	3.15 Grt*	3.11 Grt*	7.1 Grt*
Site	// S_m	// S_m	// S_m	In (St)	Late	Late	Core	Mantle	Rim	Core	Rim	Rim	Rim
SiO_2	54.76	54.59	55.21	51.93	47.53	47.68	36.89	36.86	36.61	37.28	37.58	37.53	37.37
TiO_2	0.00	0.00	0.00	0.00	0.69	0.00	0.00	0.00	0.00	0.00	0.00	0.00	0.00
Al_2O_3	25.84	25.43	25.42	28.58	37.05	40.10	21.05	20.54	20.64	20.98	21.08	20.93	21.39
FeO	2.57	2.20	2.72	2.77	0.94	0.00	34.38	35.62	35.81	34.17	31.62	29.92	30.68
MnO	0.00	0.00	0.00	0.00	0.00	0.00	2.68	0.65	1.92	1.07	0.75	0.81	0.78
MgO	4.20	4.34	4.17	3.02	0.55	0.00	1.94	2.33	2.66	0.95	1.37	1.11	1.13
CaO	0.00	0.00	0.00	0.00	0.00	0.00	2.77	3.24	1.46	5.30	7.09	9.11	8.59
Na_2O	0.00	0.50	0.00	0.59	2.33	8.40	0.00	0.00	0.00	0.00	0.00	0.00	0.00
K_2O	9.41	9.78	9.19	9.53	7.76	0.00	0.00	0.00	0.00	0.00	0.00	0.00	0.00
Total	96.78	96.85	96.71	96.42	96.84	96.18	99.71	99.24	99.10	99.75	99.48	99.42	99.93
Si	3.55	3.55	3.58	3.40	3.07	3.01	2.99	3.00	2.99	3.03	3.03	3.02	3.00
Ti	0.00	0.00	0.00	0.00	0.03	0.00	0.00	0.00	0.00	0.00	0.00	0.00	0.00
Al	1.97	1.95	1.94	2.21	2.82	2.98	2.01	1.97	1.99	2.01	2.00	1.99	2.02
Fe^{+3}	0.00	0.00	0.00	0.00	0.00	0.00	0.00	0.03	0.04	0.00	0.00	0.00	0.00
Fe^{+2}	0.14	0.12	0.15	0.15	0.05	0.00	2.33	2.39	2.40	2.32	2.13	2.02	2.06
Mn	0.00	0.00	0.00	0.00	0.00	0.00	0.18	0.05	0.13	0.07	0.05	0.06	0.05
Mg	0.41	0.42	0.40	0.30	0.05	0.00	0.23	0.28	0.32	0.11	0.16	0.13	0.13
Ca	0.00	0.00	0.00	0.00	0.00	0.00	0.24	0.28	0.13	0.46	0.61	0.79	0.74
Na	0.00	0.06	0.00	0.07	0.29	1.03	0.00	0.00	0.00	0.00	0.00	0.00	0.00
K	0.78	0.81	0.76	0.80	0.64	0.00	0.00	0.00	0.00	0.00	0.00	0.00	0.00
XMg	0.744	0.778	0.732	0.66	0.511	0.00	0.08	0.09	0.11	0.04	0.06	0.05	0.05
XFe							0.78	0.80	0.80	0.78	0.72	0.67	0.69
XCa							0.08	0.09	0.04	0.16	0.21	0.26	0.25
XMn							0.06	0.02	0.04	0.03	0.02	0.02	0.02

* Analysis used for AvPT calculations (see Table 2)

Structural formulae have been calculated on the basis of 11 oxygens for white mica and 12 oxygens for garnet.

Fe^{3+} has been calculated by stoichiometry

Table SM6b - Representative analyses of the main minerals in sample DM1565 (DSU)

	Chloritoid			Chlorite
Analysis	2.3 Cld*	2.32 Cld**	2.25 Cld	8.14 Chl
Site	In (St)	In (St)	In (St)	Late
SiO_2	25.07	24.94	25.16	24.97
TiO_2	0.00	0.00	0.00	0.00
Al_2O_3	41.12	41.39	40.95	21.77
FeO	24.15	24.13	25.23	29.31
MnO	0.00	0.00	0.00	0.00
MgO	2.80	2.89	2.52	11.99
CaO	0.00	0.00	0.00	0.00
Na_2O	0.00	0.00	0.00	0.00
K_2O	0.00	0.00	0.00	0.00
Total	93.14	93.35	93.87	88.04
Si	2.049	2.032	2.048	2.685
Ti	0.00	0.00	0.00	0.00
Al	3.959	3.974	3.928	2.758
Fe^{+3}	0.00	0.00	0.00	0.00
Fe^{+2}	1.650	1.644	1.718	2.636
Mn	0.00	0.00	0.00	0.00
Mg	0.342	0.350	0.306	1.922
Ca	0.00	0.00	0.00	0.00
Na	0.00	0.00	0.00	0.00
K	0.00	0.00	0.00	0.00
XMg	0.17	0.18	0.15	0.42

* Analysis used for AvPT calculations (see Table 2)

Structural formulae have been calculated on the basis of 14 oxygens for chloritoid and 18 oxygens for chlorite.

Fe^{3+} has been calculated by stoichiometry

Table SM7a. Independent set of reactions modelled by AvPT and used to estimate P-T conditions

Sample DM1485 (PU)	
Phe(6.1)-Grt(1.22)-Ctd(1.49)-Chl(4.7)-Qz-H_2O	Phe(2.31)-Grt(1.2)-Ctd(1.48)-Chl(4.8)-Qz-H_2O
1) ames + 2q = py + mctd + $3H_2O$	1) ames + 2q = py + mctd + $3H_2O$
2) 5alm + 5ames + 4q = 4py + 8mctd + 3daph	2) fctd + daph + 2q = 2alm + $5H_2O$
3) 23alm + 15ames + 12q = 20py + 24fctd + 9daph	3) 5alm + 5ames + 4q = 4py + 8mctd + 3daph
4) 3cel + 5alm + 3ames = 3mu + 5py + 3daph	4) 3cel + 5alm + 3ames = 3mu + 5py + 3daph
Phe(6.11)-Grt(1.21)-Ctd(2.29)-Chl(4.9)-Qz-H_2O	Phe(6.6)-Grt(1.23)-Ctd(1.33)-Chl(3.7)-Qz-H_2O
1) ames + 2q = py + mctd + $3H_2O$	1) ames + 2q = py + mctd + $3H_2O$
2) fctd + daph + 2q = 2alm + $5H_2O$	2) fctd + daph + 2q = 2alm + $5H_2O$
3) 5alm + 5ames + 4q = 4py + 8mctd + 3daph	3) 3mctd + 3daph + 6q = py + 5alm + $15H_2O$
4) 3mu + py + 2ames + 4q = 3cel + 8mctd	4) 3mu + py + 2ames + 4q = 3cel + 8mctd
5) 3cel + alm = 3fcel + py	5) 3cel + alm = 3fcel + py
Sample DM1667c (SCU)	
Phe(7.17)-Grt(2.24)-Ctd(1.5)-Lws-Qz-H_2O	Phe(10.1)-Grt(9.22)-Ctd(2.52)-Lws-Qz-H_2O
1) py + 3law = gr + 3mctd + 3q + $3H_2O$	1) py + 3law = gr + 3mctd + 3q + $3H_2O$
2) alm + 3law = gr + 3fctd + 3q + $3H_2O$	2) alm + 3law = gr + 3fctd + 3q + $3H_2O$
3) fcel + 2fctd = mu + alm + $2H_2O$	3) 3cel + 2gr + 12mctd + 6q = 3mu + 5py + 6law
4) 3cel + 2gr + 12mctd + 6q = 3mu + 5py + 6law	4) 15cel + 2gr + 12fctd + 6q = 3mu + 12fcel + 5py + 6law
Phe(10.9)-Grt(2.25)-Ctd(2.49)-Lws-Qz-H_2O	Phe(1.18)-Grt(9.1)-Ctd(2.40)-Lws-Qz-H_2O
1) py + 3law = gr + 3mctd + 3q + $3H_2O$	1) py + 3law = gr + 3mctd + 3q + $3H_2O$
2) alm + 3law = gr + 3fctd + 3q + $3H_2O$	2) alm + 3law = gr + 3fctd + 3q + $3H_2O$
3) 3cel + 2gr + 12mctd + 6q = 3mu + 5py + 6law	3) 3cel + 2gr + 12mctd + 6q = 3mu + 5py + 6law
Sample DM1281 (BIU)	
Phe(12.2)-Grt(6.3)-Ctd(5.7)-Ky-Coe-H_2O	Phe(12.1)-Grt(6b.1)-Ctd(6.49)-Ky-Coe-H_2O
1) 3fctd + 2coe = alm + 2ky + $3H_2O$	1) 3fctd + 2coe = alm + 2ky + $3H_2O$
2) 3mu + py + 4coe = 3cel + 4ky	2) 3mu + py + 4coe = 3cel + 4ky
3) 3cel + alm = 3fcel + py	3) 3cel + alm = 3fcel + py
Phe(6.88)-Grt(6.32)-Ctd(6.36)-Ky-Coe-H_2O	Phe(8.3)-Grt(10.13)-Ctd(6.33)-Ky-Coe-H_2O
1) 3fctd + 2coe = alm + 2ky + $3H_2O$	1) 3fctd + 2coe = alm + 2ky + $3H_2O$
2) 3mu + py + 4coe = 3cel + 4ky	2) pa = ky + jd + H_2O
3) 3cel + alm = 3fcel + py	3) 3mu + py + 4coe = 3cel + 4ky
	4) 3cel + alm = 3fcel + py

Table SM7b. Independent set of reactions modelled by AvPT and used to estimate P-T conditions

Sample DM1504 (RSU)

Phe(2.34)-Grt(2.2)-Ctd(2.35)-Gln(2.52)-Jd(2.44)-Lws-Qz-H_2O	Phe(6.21)-Grt(2.26)-Ctd(4.4)-Gln(2.52)-Jd(2.44)-Lws-Qz-H_2O
1) py + 3law = gr + 3mctd + 3q + $3H_2O$	1) py + 3law = gr + 3mctd + 3q + $3H_2O$
2) alm + 3law = gr + 3fctd + 3q + $3H_2O$	2) alm + 3law = gr + 3fctd + 3q + $3H_2O$
3) cel + 2mctd = mu + py + $2H_2O$	3) cel + 2mctd = mu + py + $2H_2O$
4) 3mctd + 2jd + 2q = 2pa + py + H_2O	4) fcel + 2fctd = mu + alm + $2H_2O$
5) fcel + 2fctd = mu + alm + $2H_2O$	5) 12fcel + py + 4mctd + 8jd + 4q = 5mu + 7cel + 4fgl
6) 3pa + fgl = 3fctd + 5jd + 4q + H_2O	
7) 27mu + 9cel + 4spss + 12fgl + 12law = 36fcel + 24pa + 3py + 4gr + 12mnctd	

Phe(6.16)-Grt(1.19)-Ctd(6.8)-Gln(2.52)-Jd(2.44)-Lws-Qz-H_2O	Phe(6.3)-Grt(2.1)-Ctd(2.32)-Gln(2.52)-Jd(2.44)-Lws-Qz-H_2O
1) py + 3law = gr + 3mctd + 3q + $3H_2O$	1) py + 3law = gr + 3mctd + 3q + $3H_2O$
2) alm + 3law = gr + 3fctd + 3q + $3H_2O$	2) alm + 3law = gr + 3fctd + 3q + $3H_2O$
3) cel + 2mctd = mu + py + $2H_2O$	3) cel + 2mctd = mu + py + $2H_2O$
4) 3mctd + 2jd + 2q = 2pa + py + H_2O	4) 3mctd + 2jd + 2q = 2pa + py + H_2O
5) fcel + 2fctd = mu + alm + $2H_2O$	5) fcel + 2fctd = mu + alm + $2H_2O$
6) 6fcel + 2pa + py + 2jd = 3mu + 3cel + 2fgl	6) 3pa + fgl = 3fctd + 5jd + 4q + H_2O
	7) 6fcel + 2pa + py + gr + 2acm = 3mu + 3cel + andr + 2fgl

Sample DM1565 (DSU)

Phe(5.12)-Grt(3.15)-Ctd(2.3)-Lws-Qz-H_2O	Phe(5.6)-Grt(3.11)-Ctd(2.32)-Lws-Qz-H_2O
1) py + 3law = gr + 3mctd + 3q + $3H_2O$	1) py + 3law = gr + 3mctd + 3q + $3H_2O$
2) alm + 3law = gr + 3fctd + 3q + $3H_2O$	2) alm + 3law = gr + 3fctd + 3q + $3H_2O$
3) 3cel + 2gr + 12mctd + 6q = 3mu + 5py + 6law	3) 3cel + 2gr + 12fctd + 6q = 3mu + py + 4alm + 6law

Phe(3.6)-Grt(7.1)-Ctd(2.25)-Lws-Qz-H_2O
1) py + 3law = gr + 3mctd + 3q + $3H_2O$
2) alm + 3law = gr + 3fctd + 3q + $3H_2O$
3) 3cel + 2gr + 12mctd + 6q = 3mu + 5py + 6law

Table SM8 - Mass balance of the staurolite-forming reactions

0.264 Chl + 3.496 Ky + 0.123 Grt_C = 1.000 St

	Reactants			**Products**			
Phases	Chl 6.68	Ky 6.66	Grt_C 6.15	St 6.67	Σreact	Σprod	Residuals
coeff	***-0.264***	***3.496***	***-0.123***	***1.000***			
SiO_2	2.59	1.00	2.98	3.94	-3.940	4.544	0.604
Al_2O_3	1.47	1.00	1.00	4.61	-4.610	4.006	-0.604
FeO	2.48	0.00	2.30	1.51	-1.510	0.936	-0.574
MnO	0.00	0.00	0.10	0.00	0.000	0.012	0.012
MgO	1.93	0.00	0.45	0.29	-0.290	0.564	0.274
CaO	0.00	0.00	0.14	0.01	-0.008	0.018	0.010
H_2O	4.00	0.00	0.00	1.00	-1.000	1.055	0.055

0.263 Chl + 3.712 Ky + 0.064 Grt_C = 1.000 St

	Reactants			**Products**			
Phases	Chl 11.34	Ky 11.32	Grt_C 11.6	St 11.34	Σreact	Σprod	Residuals
coeff	***-0.263***	***-3.712***	***-0.064***	***1.000***			
SiO_2	2.71	1.00	2.90	4.11	-4.110	4.610	0.500
Al_2O_3	1.56	1.00	1.00	4.69	-4.685	4.185	-0.500
FeO	2.43	0.00	2.19	1.27	-1.270	0.779	-0.491
MnO	0.00	0.00	0.10	0.00	0.000	0.006	0.006
MgO	1.75	0.00	0.54	0.26	-0.260	0.494	0.234
CaO	0.00	0.00	0.16	0.00	0.000	0.010	0.010
H_2O	4.00	0.00	0.00	1.00	-1.000	1.052	0.052

0.211 Chl + 3.620 Ky + 0.131 Grt_M = 1.000 St

Reactants				**Products**			
Phases	Chl 6.52	Ky 6.53	Grt_M 6.21	St 6.50	Σreact	Σprod	Residuals
coeff	***-0.211***	***-3.620***	***-0.131***	***1.000***			
SiO_2	2.77	1.00	2.99	4.04	-4.040	4.598	0.558
Al_2O_3	1.33	1.00	1.00	4.59	-4.590	4.032	-0.558
FeO	1.56	0.00	2.05	1.23	-1.230	0.599	-0.631
MnO	0.00	0.00	0.08	0.00	0.000	0.010	0.010
MgO	3.01	0.00	0.67	0.46	-0.460	0.724	0.264
CaO	0.00	0.00	0.17	0.00	0.000	0.022	0.022
H_2O	4.00	0.00	0.00	1.00	-1.000	0.846	-0.154

Reactions were balanced using the least-squares method. Stoichiometric coefficients and compositions are expressed in moles. *Σreact*: overall composition of the reactants; *Σprod*: overall composition of the products; *Residuals:* residual vector from the method of least squares (molar bulk composition of the product - molar bulk composition of the reactants).